PREDICTING PEAK LOAD OF THE FEMORAL NECK USING STRUCTURAL PARAMETERS

BY

ERIC J. CURRIER

THESIS

Submitted in partial fulfillment of the requirements
for the degree of Master of Science in Mechanical Engineering
in the Graduate College of the
University of Illinois at Urbana-Champaign, 2016

Urbana, Illinois

Adviser:

Assistant Professor Mariana Kersh

ABSTRACT

The current clinical standard for diagnosing osteoporosis uses measurements of bone mineral density (BMD) by dual energy X-ray absorptiometry (DXA). This measurement only partially explains the strength of bones and fails to incorporate other factors that alter bone quality. The aim of this study was to investigate how micro and macro cortical bone structures along the length of the femoral neck relate to the peak load of the proximal femur. Structural measurements were taken from microCT images of ten murine right femurs at ten locations along the femoral neck. These specimens were then tested to failure. The major diameter, minor diameter, cortical thickness, cross sectional area, cortical area, and cortical fraction were measured and correlated to the peak compressive load. The highest significant correlation was found using major diameter ($R^2 = 0.6$) or cross sectional area ($R^2 = 0.59$). Significant correlations for the major diameter were found between 40% - 60% along the femoral neck, while cross sectional area had significant correlations between 40% - 80% of the femoral neck. By combining major diameter and cortical area in a multivariable regression, R^2 improved to 0.66. Understanding the contribution of cortical structure to peak load will allow for improved characterization of bone properties in both healthy and diseased bone, and provide indices for targeted imaging to better diagnosis osteoporosis.

ACKNOWLEDGMENTS

I would like to express my sincere appreciation to Mariana Kersh for her assistance in the development and completion of this thesis. In addition, I would like to thank Marina Marjanovic for supplying the mice specimens, LeiLei Yin for training me on the microCT scanner, and Kevin Brenner for his support on this project.

TABLE OF CONTENTS

CHAPTER 1: INTRODUCTION

Osteoporosis is a disease that affects millions of Americans and results in the deterioration of bone strength and an increased likelihood of bone fracture (Cummings & Iii 2002; Sernbo & Johnell 1993). The incidence of osteoporosis is expected to increase due to the growth in the elderly population. It is projected that from 2010 to 2040 the population of persons over 65 years of age will double (Cooper et al. 2011). The cost of osteoporotic fractures is approximately $20 billion per year in the United States (Op Den Buijs & Dragomir-Daescu 2011; Burge et al. 2007). Among these fractures, 250,000 are reported as hip fractures (Florschutz et al. 2015). The elderly population is most susceptible to hip fractures due to the decreased bone strength caused by osteoporosis and the increased risk of falling (Op Den Buijs & Dragomir-Daescu 2011). These fractures can lead to higher levels of mortality and morbidity, reduce the overall quality of life, and impose an economical burden. Importantly, hip fractures in the elderly have been associated with the highest mortality and morbidity rates (Sernbo & Johnell 1993).

The current clinical standard for diagnosing osteoporosis uses measurements of bone mineral density (BMD) by dual energy X-ray absorptiometry (DXA). This measurement only partially explains the strength of bones and fails to incorporate other factors that alter bone quality (Ito 2011; Wainwright et al. 2005; Mccreadie & Goldstein 2000; Absorptiometry & Nielsen 2000). Alone, BMD has a correlation of approximately 50% with fracture load (Cody et al. 1999; Lochmüller et al. 2000). In trabecular bone, measurements of BMD fail to explain 90% of the bone quality (Ciarelli et al. 1991). Bone quality therefore includes other factors that are assumed to influence bone strength including bone architecture, bone cell distribution, bone remodeling, distribution of microcracks, and bone matrix properties (Bouxsein 2003; Felsenberg & Boonen 2005; Seeman & Delmas 2006).

Bone morphological parameters, and their relation to strength, have been receiving more attention in the literature. Several studies have reported measurements of strength with changes in femoral neck cross-sectional area, cortical thickness, cortical area, porosity, degree of

anisotropy, and other trabecular parameters (Kersh et al. 2013; Müller 2009; Perilli et al. 2007). However, these studies have been limited by (1) simplified bone morphology, (2) assumed constitutive models and properties, (3) surface cortical strain measurements, or (4) small excised samples of bone (Kersh et al. 2013; Natali & Meroi 1989; Peng et al. 2006; Zysset 2003; Helgason et al. 2008; Sztefek et al. 2010; Schileo et al. 2007; Gillard et al. 2014; Wentzell et al. 2015). Therefore, there is the need to investigate how, and to what degree, micro and macro structural parameters and material property information contribute to bone strength using robust experimental measurements of strength.

The quantification of structural parameters in the proximal femur can provide information about hip fracture risk. Specifically, the femoral neck is of interest due to its correlation to fracture loads and high incidence among osteoporotic fractures (Lotz et al. 1995; Courtney et al. 1995; Esses et al. 1989; Lotz & Hayes 1990). The objective is to investigate how bone architecture and material properties of the femoral neck relate to full-field three-dimensional strain measured by DVC. The first aim of this objective, which has been completed in this study, is to quantify the cortical bone structural parameters of the femoral neck and relate them to macro level mechanical properties. Understanding the contribution of cortical architecture to strength will allow for an improved characterization of bone properties in both healthy and diseased bone, and provide indices for targeted imaging to better diagnosis osteoporosis.

CHAPTER 2: LITERATURE REVIEW

2.1 Bone Structure and Composition

Bone is a complex, heterogeneous, and hierarchical material that provides a framework for the skeletal system, serves as the attachment site for muscles, tendon, and ligaments, and protects vital organs. In addition, bone stores calcium (mineral homeostasis) and forms blood cells (hematopoesis) (Bouxsein 2003). The unique structure of bone at different length scale influences the bone mechanical and material properties (Rho et al. 1998; Cristofolini et al. 2008; Ding et al. 1997; Grassi & Isaksson 2015). Adapted from the structural arrangement proposed by Rho, the bone is organized into six distinct levels (Fig. 2.1) (Rho et al. 1998):

1. Macrostructure: whole bone
2. Mesostructure: trabecular and cortical bone
3. Microstructure (from 10 to 500 μm): Haversian systems, osteons, single trabeculae
4. Sub-microstructure (1 – 20 μm): lamellae, lacunae, and cement lines
5. Nanostructure (from a few hundred nanometers to 1 μm): collagen and embedded mineral
6. Sub-nanostructure (below a few hundred nanometers): mineral, collagen, and non-collagenous organic proteins

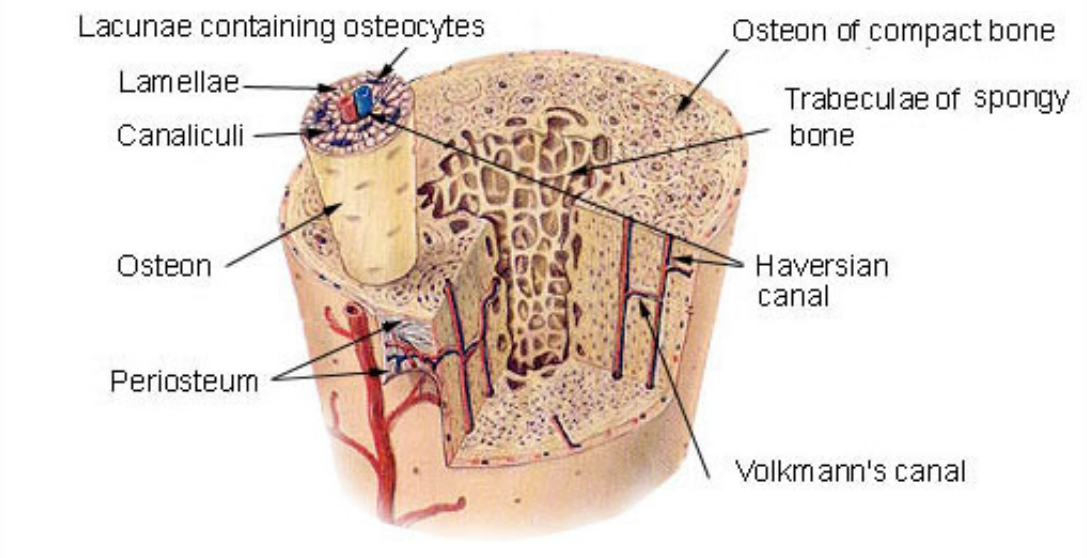

Figure 2.1: The cross section of a long bone shows various length scales and how they are organized. At level 2, trabecular bone resembles a spongy network seen in the center of the bone and cortical bone is the compact outer bone. Level 3 osteons and trabeculae are identified as well as level 4 lamellae and lacunae (SEER 2011).

Bone is classified as either cortical (cancellous) or trabecular (cancellous) bone at the mesostructural level. Cortical bone is the hard outer shell of all bones, making up approximately 85% of the skeleton (Bagi et al. 2006). Trabecular bone is found in the epiphyseal region of long bones and makes up the core of flat bones and vertebrae. Cortical and trabecular bone can also be categorized by porosity. Trabecular bone has a porosity up to 90% while cortical bone has a porosity of 3% to 5% (Natali & Meroi 1989). However, it has been found that cortical bone porosity can be as high as 24% to 28% in elderly individuals (Wang & Ni 2003). The heterogeneity of bone structure continues to the microstructure level.

Osteons are the principal structural unit of cortical bone, while trabeculae are the principal unit of trabecular bone. Osteons are composed of a central Haversian canal housing capillaries and nerves, surrounded by concentric lamellae while trabeculae form an avascular network of rods and/or plates with less organized lamellae (Rho et al. 1998). Lamellae are organized sheets of mineralized collagen. The individual constituents of lamellae are Type 1 collagen and inorganic

apatite crystals (Felsenberg & Boonen 2005). The mineral provides stiffness and strength, and the collagen contributes to ductility and toughness (John 2003; Seeman & Delmas 2006).

2.2 Mechanical Properties of Bone

In Mucnckhof's study, he presents a table gathered from previous studies of experimentally measured human proximal femur fracture loads (Van Den Munckhof & Zadpoor 2014). From a study completed by Cody, the highest fracture load in the stance position of the femoral neck was 9196 N ± 3177 N (Cody et al. 1999). The lowest femoral neck fracture load listed was 4448 ± 1541 N in the stance position and was completed by Keyak (Keyak et al. 1998). Buijs, who was not included in Munckhof's table, reported the stiffness and fracture load of the proximal femur as 1694 ± 482 N/mm and 4441 ± 1558 N, respectively (Op Den Buijs & Dragomir-Daescu 2011).

In this study, mice specimens are being investigated, so it is relevant to know mechanical properties of murine femurs. The peak load of the femoral neck was reported as 18.6 ± 4.1 N and 18.9 ±3.5 N in two studies (Jämsä et al. 1998; Jämsä et al. 1999). The stiffness of murine femurs range from 89.7 ± 9.2 N/mm to 118 ± 3 N/mm in high bone mineral density (BMD) specimens and 51.2 ± 6.9 N/mm to 90 ± 5 N/mm in low BMD specimens (Voide et al. 2008; Turner et al. 2000).

The majority of mechanical properties of the proximal femur are measured by static loading of the femoral head (Van Den Munckhof & Zadpoor 2014; Cody et al. 1999; Keyak et al. 1998; Op Den Buijs & Dragomir-Daescu 2011; Turner et al. 2000). The loading configuration can be altered, but the setup and preparation vary only slightly.

2.3 Bone Quality

Clinically, bone quality is assessed using dual x-ray absorptiometry (DXA) measurements, which provide an index of bone mineral density. Unfortunately, DXA-based measurements do not fully explain the strength of bones (Ito 2011; Imai 2015; Mccreadie & Goldstein 2000;

Nielsen 2000). Areas with comparable BMD, but differing architecture may have up to a 50% difference in strength and stiffness (Galante et al. 1970; Cole & Van Der Meulen 2011).

Many studies measure the known and unknown properties (Table 2.1) that influence bone strength as bone quality (Cole & Van Der Meulen 2011; Bouxsein 2003; Felsenberg & Boonen 2005). Table 2.1 focuses on the different structural parameters of cortical and trabecular bone that have been quantified.

Table 2.1: Parameters of Bone Quality

Level	Parameter	Study
Cortical geometry	Cross sectional area	(Beck et al. 2000; Filardi et al. 2004; Nelson et al. 2004; Wang et al. 2005; Kersh et al. 2013)
	Cortical thickness	(Beck et al. 2000; Filardi et al. 2004; Theobald et al. 1998; Wang et al. 2005; Yoshikawa et al. 1994; Kersh et al. 2013)
	Cortical area	(Kersh et al. 2013)
	Porosity	(Bousson et al. 2004)
	Cortical outer diameter	(Nelson et al. 2004; Theobald et al. 1998; Yoshikawa et al. 1994; Kersh et al. 2013; Cody et al. 1999)
	Cortical fraction	(Kersh et al. 2013)
Trabecular architecture	Thickness	(Perilli et al. 2007; Hildebrand et al. 1999; Cristofolini et al. 2009)
	Trabecular number	(Hildebrand et al. 1999)
	Connectivity	(Odgaard & Gundersen 1993)
	Bone volume	(Hildebrand et al. 1999; Hahn et al. 1992)
	Bone volume fraction	(Perilli et al. 2007; Hildebrand et al. 1999)
	Trabecular separation	(Perilli et al. 2007; Hildebrand et al. 1999)

An increase in cortical outer diameter has been shown to increase bone strength. Cortical thickness has also been shown to increase bone strength but to a lesser extent than cortical diameter (Ammann & Rizzoli 2003). Cortical thinning and increased cortical porosity leads to decreased bone strength (Pistoia et al. 2003; Bousson et al. 2004). The ratio of bone volume to total volume (BV/TV) and apparent density has been shown to explain 60% - 85% of the

apparent stiffness and strength of human trabecular bone in compression (Keaveny et al. 1997; Kopperdahl & Keaveny 1998; Liu et al. 2010; Morgan et al. 2003). Parfitt predicted that the loss of trabeculae has a greater influence than trabecular thinning on bone strength (Parfitt 1992). Mittra found that BV/TV correlates with ultimate strength ($R^2 = 0.81$), yet structural model index (SMI) correlates slightly higher ($R^2 = 0.85$) than BV/TV (Mittra et al. 2005). Additionally, properties such as connectivity density or degree of anisotropy were less able to predict the mechanical properties of bone than trabecular number, thickness, and spacing. This supports the claim that structural indices are important for predicting bone strength if not more important than material density oriented indices (Mittra et al. 2005).

Bone quality parameters can be measured from microCT images and be used to describe the whole bone or local sections on the micron scale (Kersh et al. 2013; Bagi et al. 2006). Better understanding of the relationship between structural parameters and strain can provide insight into how bone responds to loads. However, just as quantifying bone quality has it challenges, measuring the strain of bone can be difficult.

2.4 Local Strain Measurements

Strain gauges are used to measure the strain between two points using electrical resistance. As the strain increases, the electrical resistance of a wire will increase and as the strain decreases the electrical resistance will decrease (Yang et al. 2011). A single strain gauge can measure strain in one direction, however, by combining multiple gauges, a rosette strain gauge can be created allowing simultaneous measurements in multiple directions.

Strain gauges were used on bone shortly after being introduced in the literature and remain the gold standard for strain measurements on bone (Wentzell et al. 2015; Grassi & Isaksson 2015; Yang et al. 2011). A main advantage to using strain gauges is that it allows for in vivo studies, a majority of which focus on the human tibia (Lanyon et al. 1975; Burr et al. 1996; Yang et al. 2011). Strain gauges have also been used to measure strains in other bones and in different species (Field & Rushton 1989; Cristofolini et al. 2009; Bessho et al. 2007; Schileo et al. 2007; Földhazy et al. 2005; De Souza et al. 2005; Sztefek et al. 2010).

Cristofolini investigated the strain distribution in eleven locations on the human femoral metaphysis under loading conditions modeled from different physiological activities (walking, single leg stance, stair climbing, and standing from seated position) (Cristofolini et al. 2009). The average principal strain of all loading configurations and strain gauge measurements under 0.75 of body weight (body weight (BW) was unique to each specimen) was between 217 με and -309 με (Cristofolini et al. 2009). Low impact activities such as level walking, single-leg stance, and stair climbing produce joint contact forces between the hip and femur range from 1.9 to 2.6 BW (Bergmann et al. 2001). Cristofolini extrapolated his findings to Bergmann force levels, resulting in predicted average principal strains from 725 με and -1029 με (Cristofolini et al. 2009). Events such as stumbling can result in hip contact forces as high as 7.2 – 8.7 BW and strains of 5762 με or more (Bergmann et al. 1993; Bergmann et al. 2004; Cristofolini et al. 2009). Strains in murine models are important because it allows for more controlled experimental evaluations of the effect of exercise, disease state, genetic manipulation, and pharmaceutical therapies on bone. The strains in the medial tibia of murine specimens have been reported as 0.166% ± 0.01% in the medial tibia of murine specimens, while De Souza reported strains ranging from -0.1% to -0.2% in the lateral tibia of murine specimens (Sztefek et al. 2010; De Souza et al. 2005).

Although strain gauges have been used extensively, they only provide strain measurements at a limited area of the bone (Cordey & Gautier 1999a; Cordey & Gautier 1999b; Sztefek et al. 2010). The invasive procedure of applying strain gauge should be further investigated in in vivo studies to determine if the application changes the gait of those individuals. Furthermore, strain gauges must be bonded at a flat surface and can artificially increase the stiffness of its site known as the "reinforcement effect" (Grassi & Isaksson 2015; Perry 1986).

2.5 Computational Methods for Strain Predictions

Finite element (FE) models constructed from computed tomography (CT) scans allows the estimation of bone strength, fracture risk, and strain throughout bone (Cody et al. 1999; Huiskes

& Chao 1983; Prendergast 1997; Peng et al. 2006; Martelli et al. 2014). CT scans can be used to tailor models to individual patients (Keyak et al. 1993; Schileo et al. 2007).

Martelli used an FE model of the right femur to investigate the effect of different physical activities on the strain energy and peak tensile strain. Maximum values of peak strain energy (0.29 J) and peak tensile strain (0.51%) occurred during maximum isokinetic hip-extension (Martelli et al. 2014). Overall, strain ranged from 0.10% to 0.51%, corresponding to 13% and 70% of the theoretical fracture threshold (Martelli et al. 2014).

The accuracy of finite element models is an important consideration when interpreting results. Cody reported FE analyses with an $R^2 = 0.84$ compared to actual measured fracture load, while Keyak developed a nonlinear FE model with a correlation coefficient (r) of 0.962 (Cody et al. 1999; Keyak 2001). Van Den Munckhof determined the accuracy of several FE models able to predict the fracture load of the proximal femur found in the literature (Van Den Munckhof & Zadpoor 2014). This study suggested that the reviewed models varied from experimental results by 5% - 46% with a majority of the studies falling between 10 and 20% (Van Den Munckhof & Zadpoor 2014).

A limitation of FE models is the simplification of bone material properties, geometry, and loading conditions, possible resulting in errors in strains predictions (Sztefek et al. 2010). Furthermore, the literature contains several density–elasticity laws with little consensus on the optimal constitutive model (Linde et al. 1992; Natali & Meroi 1989; Peng et al. 2006; Zysset 2003; Helgason et al. 2008). However, the experimental measurements with which to validate finite element models are limited and their acquisition remains a challenge for successful model development.

2.6 Optical Measurements of Strain: Digital Image Correlation

Digital image correlation (DIC) is an optical technique for measuring the surface strain of a material by tracking high contrast speckles with high-resolution cameras. DIC was originally designed to measure large displacements, however, with the advancement of optical technology,

it has become possible to track strains at the micro level (Grassi & Isaksson 2015). In addition to measuring full field surface strains, the application of a minimum-contact speckled pattern removes the possibility of direct measurement artifacts (Tang et al. 2015). The use of DIC has increased in recent years for measuring biological tissue strains (Christen et al. 2012; Dickinson et al. 2012; Sztefek et al. 2010; Thompson et al. 2007; Wentzell.S, Nesbitt. R.S, Macione.J, Knapp. R 2011).

Gilchrist investigated the accuracy of DIC by comparing DIC measured strains to those measured by strain gauges (Gilchrist et al. 2013). DIC accurately predicted the strain of the human femur under 50% of their predicted fall fracture load (root mean square difference = 127 με and standard deviation = 239 με) (Gilchrist et al. 2013). Using DIC, Sztefek measured the mean medial strain to be 0.144 ± 0.042 and the mean lateral strain to be -0.050 ± 0.011% in murine tibiae (Sztefek et al. 2010). These values did not significantly differ from previously reported medial mean strain values measured by strain gauges (Sztefek et al. 2010). Carriero measured peak and average strain on the medial surface of two murine tibiae. Average strain was 0.26 ± 0.038% and 0.255 ± 0.033% for the left and right leg, respectively (Carriero et al. 2014). Peak strain was 0.454 ± 0.054% and 0.465 ± 0.044% for the left and right leg, respectively (Carriero et al. 2014).

Although DIC is able to measure surface strains, it is unable to provide internal volumetric measurements. These volumetric strains are important to understand how different micro and macro structures affect bone fracture. Another limitation of this method is that it assumes objects being measured have no discontinuities in displacement between consecutive images (Grassi & Isaksson 2015).

2.7 Optical Measurements of Strain: Digital Volume Correlation

Digital volume correlation (DVC) is the three-dimensional equivalent of DIC and was first introduced by Bay. DVC computes the three-dimensional internal strain of an object by measuring the displacement of a sub-volume between a reference and deformed image set. The sub-volume is tracked between these images using the images' natural variation of grayscale

values. This process is reliable if the object has a distinct internal pattern that is not excessively deformed. DVC has been used to measure the internal strain of trabecular bone (Bay et al. 1999; Gillard et al. 2014; Liu & Morgan 2007), scaffolds (Madi et al. 2013), bone implant interfaces (Basler et al. 2011), and whole vertebrae (Hussein et al. 2012).

Gillard studied the compressive behavior of porcine trabecular bone extracted from the femoral head using DVC (Gillard et al. 2014). Applying an absolute displacement of 6.8 mm, the maximum internal strains ranged from 0.5 – 0.9% with a resolution of 0.02 – 0.08%. These finding are consistent with failure strains of trabecular bone in previous studies (Kopperdahl & Keaveny 1998). Hussein used DVC to detect the onset and progression of failure in an intact human vertebra with a mean displacement and strain of 21.56 ± 41.44 μm and 740 ± 630 με, respectively (Hussein et al. 2012). Unfortunately, Hussein reported errors higher than previous studies (Liu & Morgan 2007; Hardisty 2009).

DVC is a powerful imaging advancement in the quantification of local internal strain of bone; however, it has several limitations that must be investigated before practical application. First, specimens must have an intrinsic pattern and loading conditions should not result in excessive deformation. The results of DVC need to be validated, as the choice of subset size can influence the precision of DVC results (Jandejsek et al. 2011). Dallara reviewed the finding of several studies and found that the accuracy and precision of strain varies from 20 – 1280 με and 39 – 639 με, respectively (Dall'Ara et al. 2014). Lastly, the optimal image resolution for DVC has not yet been determined (Grassi & Isaksson 2015).

2.8 Opportunities for Improvement

Understanding the mechanics of bone and bone strength has been limited by (1) simplified bone morphology, (2) assumed properties and constitutive models, (3) surface cortical strain measurements, or (4) the use of small excised samples of bone (Kersh et al. 2013; Natali & Meroi 1989; Peng et al. 2006; Zysset 2003; Helgason et al. 2008; Martelli et al. 2014; Van Den Munckhof & Zadpoor 2014; Sztefek et al. 2010; Schileo et al. 2007; Yang et al. 2011; Cristofolini et al. 2009; Gillard et al. 2014; Wentzell et al. 2015; Mittra et al. 2005).

Helgason performed an extensive review comparing various mathematical models correlating Young's modulus with apparent density finding little consensus amongst studies and recommending that experimental methodology and anatomical site be considered when choosing an elasticity-density relationship (Helgason et al. 2008). By implementing the Morgan constitutive mathematical model, Schileo reports to have successfully created a subject-specific FE model that mimics experimental strains in the femur (Morgan et al. 2003; Schileo et al. 2007). One of the limitations is that the subject-specific FE model utilized a single density-elasticity for the entire range of bone densities (Schileo et al. 2007). Martelli created an in-depth model that incorporated the bone geometry from a CT scanner and the musculoskeletal anatomy from an MRI to investigate the effect of different physical activities on the strain energy and peak tensile strain (Martelli et al. 2014). These models rely on past experimental work to predict the behavior of simulated environments. The amount of variation between studies and the lack of quantified geometric or material properties limit the interpretation of these models though.

Experimental work is not without its challenges as measuring the desired results can prove fundamentally challenging. To measure the in vivo bone strain in humans under physiological loading, Yang and Cristofolini bonded strain gauges directly to the bone, which is limited to a small area on the surface (Yang et al. 2011; Cristofolini et al. 2009). Sztefak measured the entire surface strain of a mouse tibia using DIC, but is unable to capture the internal volumetric strain (Sztefek et al. 2010).

Using DVC, Gillard analyzed the strain in a cube of cancellous bone from the femoral head of a porcine femur and Wentzell measured strain fields on quartered mid shafts of human femurs (Gillard et al. 2014; Wentzell et al. 2015). These studies are limited to small bone samples excised from their natural mechanical environments, which can lead to non-physiological strain patterns. To the authors knowledge only two studies have investigated internal three-dimensional strain of whole bone (Hussein et al. 2012; Hardisty 2009). Hussein investigated three-dimensional deformation of whole, intact, human vertebral, while Hardisty investigated whole, intact, rat-tail vertebra (Hussein et al. 2012; Hardisty 2009).

Bone is a complex, hierarchical material that can be difficult to quantify; however, advances in imaging provide new techniques to accurately quantify bone morphology and material properties. There remains the need to study the three-dimensional mechanical response of whole, intact femur and how local and global mechanics relate to micro and macro structural properties.

CHAPTER 3: EXPERIMENTAL METHODS

3.1 Specimen Preparation

Ten C57/B16 normal mice were used in this study ranging in age from 8 to 14 months (Table 3.1). Mice were stored at -25°C and thawed at room temperature. The right femurs were dissected and all soft tissue surrounding the bone was removed. The specimens were wrapped in PBS soaked gauze during storage and testing to ensure hydration.

Table 3.1: Mice Specimen Information

Specimen	Gender	Femur	Mouse Length (mm)	Mouse Weight (g)	Femur Length (mm)	Femur Weight (g)
1	F	R	88.06	23.026	15.64	0.064
2	M	R	97.02	34.043	15.27	0.074
3	F	R	97.15	26.573	15.43	0.068
4	F	R	95.96	28.072	15.90	0.073
5	M	R	85.76	41.462	14.48	0.067
6	F	R	77.18	20.539	14.67	0.059
7	F	R	79.36	22.154	15.08	0.065
8	M	R	75.75	29.905	14.76	0.065
9	F	R	80.33	23.091	14.10	0.068
10	F	R	92.90	36.887	15.21	0.068

3.2 Potting with Custom Fixtures

Femurs were potted with DAP® Plaster of Paris in custom 6061 aluminum fixtures compatible with the testing stage (Fig. 3.1A). The base fixture was designed to securely pot the whole femur. The depth of the cup allowed for over half the length of the femur to be potted and the designed top grooves prohibited rotational movement. The top fixture used the same cup design, but had a different connector interface due to the constraints of the testing stage (Fig. 3.1B). Furthermore, the specimen was not potted in the top fixture, but rather imprinted.

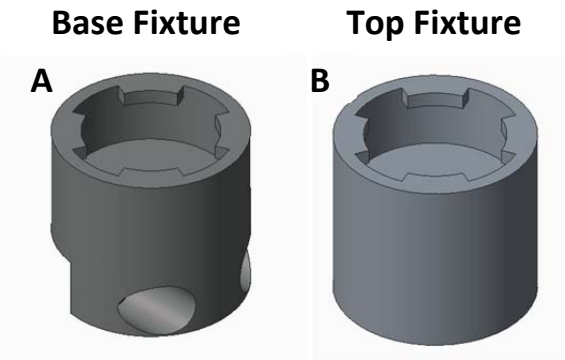

Figure 3.1: (A) The femur was potted in the aluminum base fixture, which fastened to the testing stage crosshead. (B) A specimen specific imprint was created in the top fixture to reduce local crushing and slipping.

To reduce bending, slipping, and local crushing at the femoral head, an imprint of each femoral head is created in a DAP® Plaster of Paris filled top fixture. The shallow imprint decreased local crushing by increasing the surface contact with the femoral head. The loose "ball and socket joint" formed by the imprint and femoral head held the femur in position during testing.

The top and bottom fixture are not connected, so a custom rig, modeling the testing stage, was machined to accurately position the top and bottom fixture (Fig. 3.2). This 6061 aluminum custom rig consists of an outer housing guide (Fig. 3.2A), sliding key (Fig. 3.2B), and a baseplate (Fig. 3.2E). The base fixture (Fig. 3.2C) connects to the sliding key and the top fixture (Fig. 3.2D) connects to the baseplate. The sliding key and housing key ensure that the two fixtures have an angle offset of 10.19° (measured from the mechanical testing stage).

Once the femur was initially set in the base fixture (~20 minutes), the imprinting procedure was started. The top fixture was connected to the baseplate and filled with DAP® Plaster of Paris (Fig. 3.3A). The plaster was allowed to settle between 5 to 10 minutes at which point the surface plaster was hard, yet still deformable. This subassembly (top fixture and baseplate) was then securely fastened to the housing guide (Fig. 3.3B). The base fixture was connected to the sliding key and lowered into the housing guide (Fig. 3.3C). A strip of nitrile rubber cut from a disposable glove was placed over the top fixture to prohibit direct contact of the femoral head with the plaster. The sliding key and base fixture were gently lowered until the femoral head

contacted the nitrile barrier (Fig. 3.4). The base fixture and sliding key were released and the weight of this subassembly imprinted the femoral head into the top fixture. After imprinting, all parts were disassembled and both fixtures were allowed to fully settle for a minimum of 18 hours. Excluding the actual imprinting step, the femur was wrapped in PBS soaked gauze for the duration of the procedure.

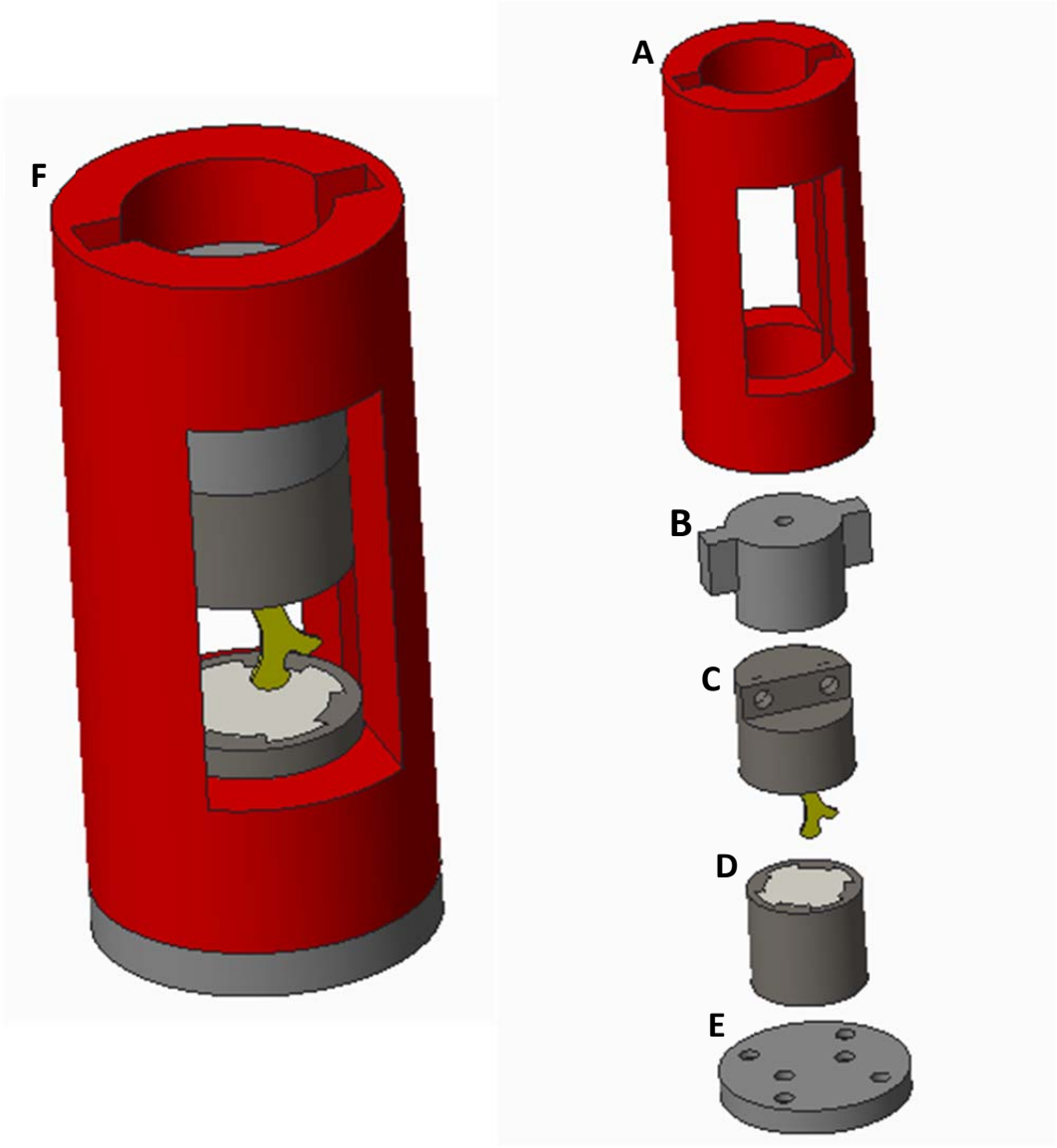

Figure 3.2: (A-E) The exploded 3D assembly of the imprinting rig. (F) The fully assembled imprinting rig including a sample femur.

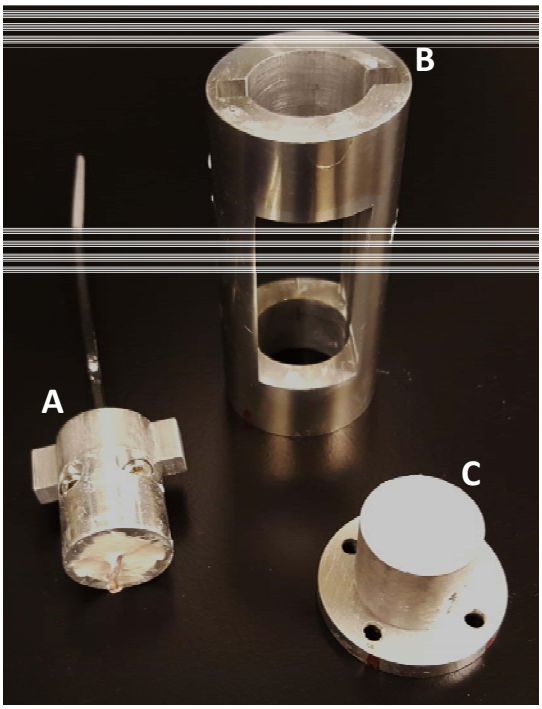

Figure 3.3: (A) The base fixture with potted femur is connected to the imprinting key. A cord is fastened to this subassembly to assist in lowering the structure onto the top fixture. (B) The housing guide that will be used for accurate and consistent imprints. (C) The top fixture and base plate filled ready to begin the imprinting step.

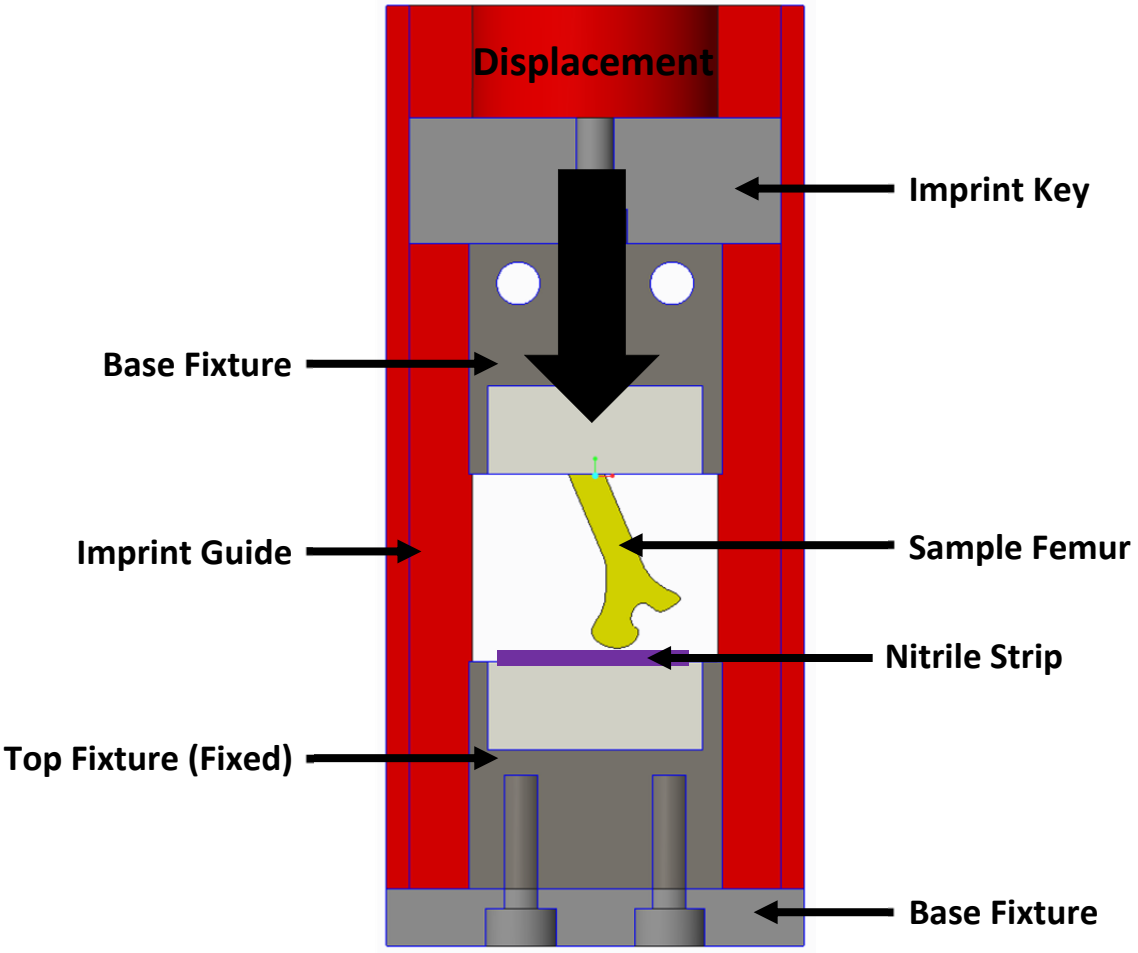

Figure 3.4: Cross section of assembled 3D imprinting rig during the imprinting step.

3.3 Mechanical Testing

Mechanical tests were performed using a Deben CT500 500 N in-situ tensile and compression stage for μXCT applications (Fig. 3.5). The custom imprinted top fixture and the potted specimen base fixture were rigidly mounted to the testing stage. For the low-force step mechanical test, the Deben testing stage was zeroed and 2 N of compressive force was axially applied to the femur at a rate of 0.2 mm/min. The bone was held fixed once 2 N was reached and CT scanned. After the first scan, the load was increased to 7 N of compressive force at a rate of 0.2 mm/min. The bone was again held fixed once 7 N of force was reached and CT scanned.

Once scanning was completed, specimens 5 through 10 were unloaded and allowed to rest for 10 minutes. The bone was then tested to failure at a rate of 0.2 mm/min. Specimens 1 through 4 underwent the low-force step mechanical test, but were then stored between 20 to 30 days before being tested to failure at a rate of 0.2 mm/min. Refer to Appendix A for full force-displacement curves of the step mechanical test.

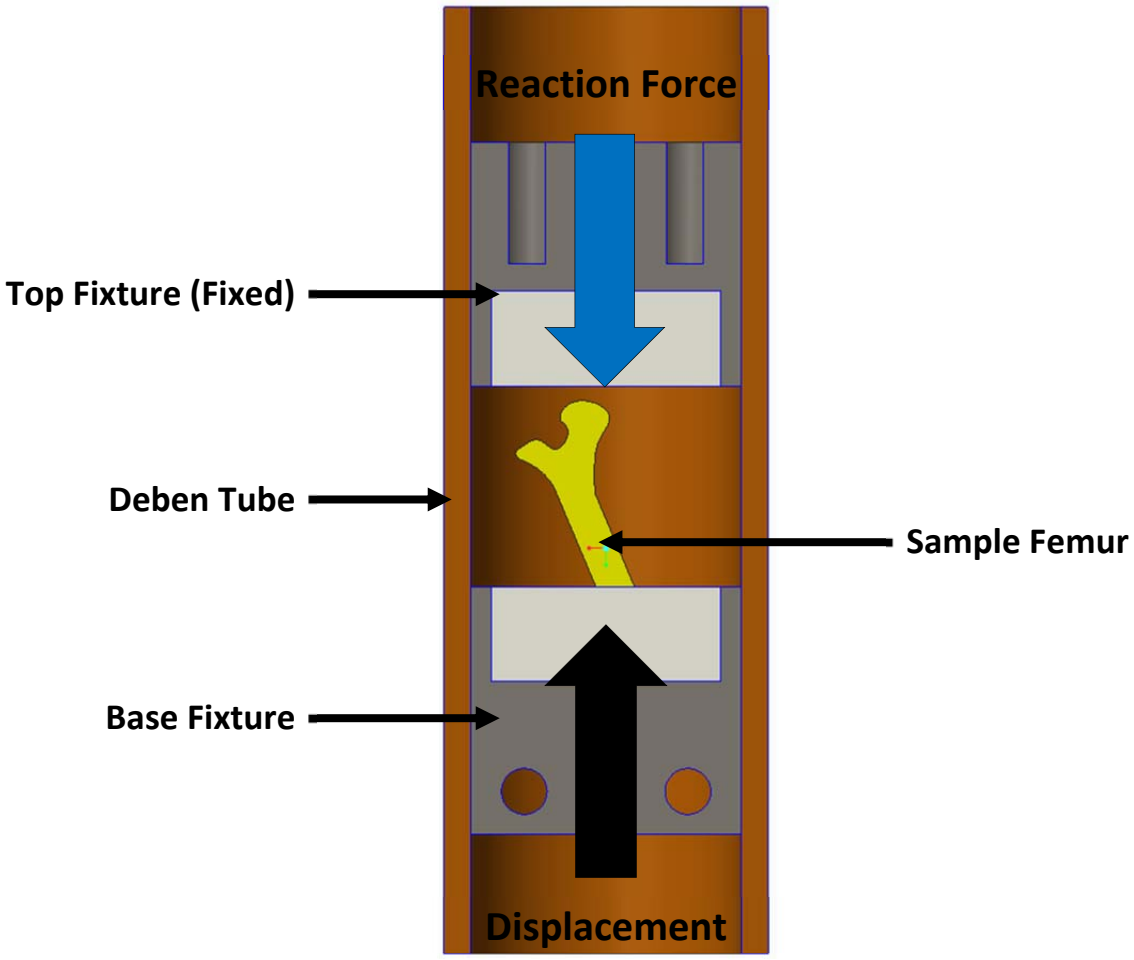

Figure 3.5: The Deben testing stage loading configuration including a sample femur.

3.4 MicroCT Imaging

MicroCT scanning was completed using an Xradia MicroXCT-400 at an isotropic resolution of 3.77 microns. Once the fixtures were fastened into the Deben, the Deben was secured on the scanning stage (Fig. 3.6). Each scan yielded an image stack of 996 images with a height of 1016

pixels and a width of 996 pixels. Initially, 361 projection images were taken at 10 second intervals, however, to reduce noise this was increased to 722 projection images. These projections were taken over a 2 hour and 42 minute period at a voltage and current of 3 0kW and 200 mA, respectively. For complete microCT parameters and image stack information, please reference table 3.2 and 3.3, respectively.

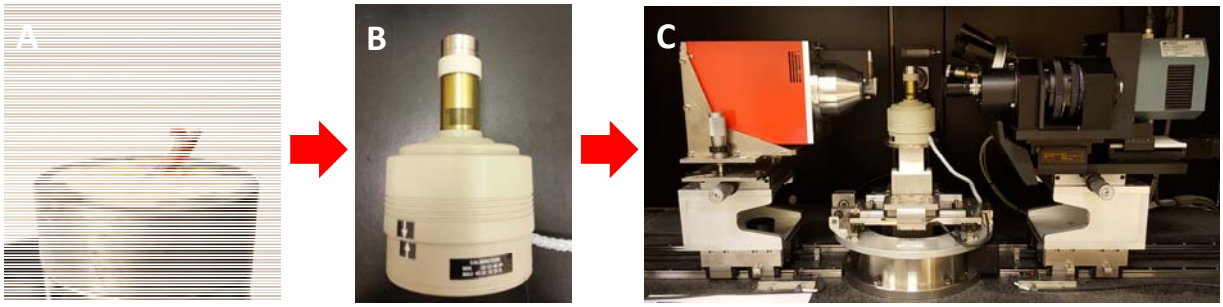

Figure 3.6: (A) The base fixture with the potted femur was fastened in the (B) Deben mechanical testing stage. (C) The testing stage was secured to the scanning stage inside the microCT scanner.

Table 3.2: MicroCT Parameters

Source Parameters		Detector Parameters	
Position (mm)	-77	Position (mm)	60
Power (W)	6	Magnification	4
Current (kV)	30	FOV (mm)	2.4 – 6
Voltage (mA)	200		
Exposure Time (sec)	10		

Table 3.3: Image Stack Information

Scan Size	
x (pixels)	996
y (pixels)	1016
z (pixels)	996
Voxel Size (µm)	3.7744

During the step mechanical testing, the CT scans were delayed by ten minutes once the desired force increment was reached to allow for settling and reorganization of the bone. Figure 3.7

illustrates the CT scanner timeline including the mechanical test. The ultimate load test is not included in this timeline because the CT scanner was not active during this test.

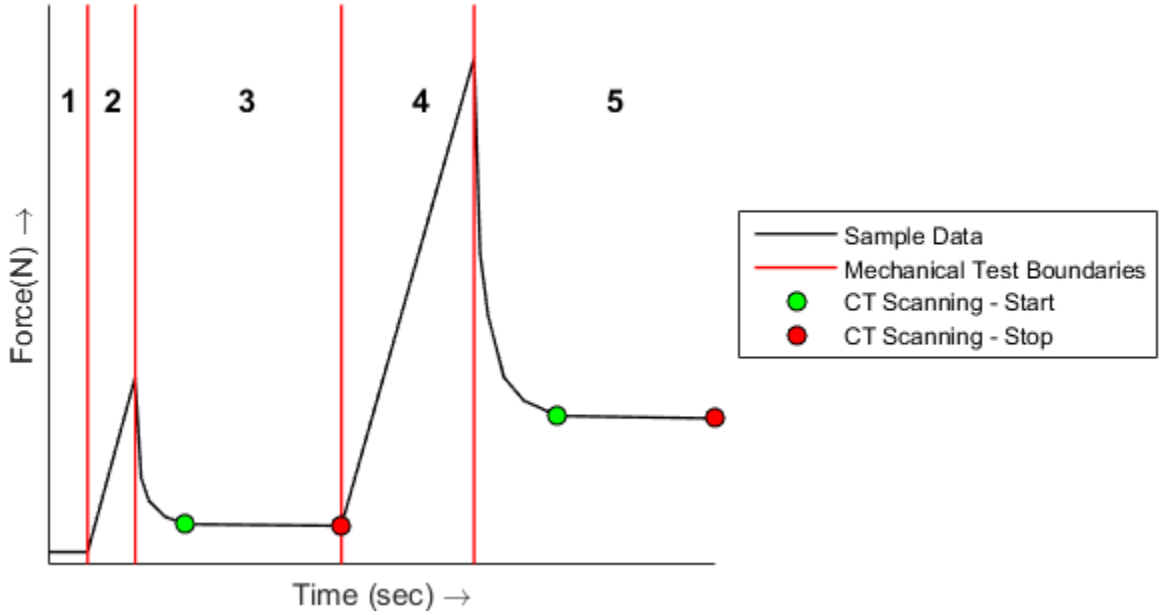

Figure 3.7: The model force versus time CT procedure. (1) This beginning zone is before the imprinted top fixture contacts the femoral head. (2) The loading of the bone to 2 N at a constant rate of 0.2 mm/min. (3) The crosshead remained fix as the bone reorganized and a scan was taken. Before starting the first scan, a 10 minute delay was established to limit the drop in force once the scan started. (4) The loading of the bone to 7 N at a constant rate of 0.2 mm/min. (5) Before starting the second scan, another 10 minute delay was established to limit the drop in force.

Although CT scans were taken at 2 N and 7 N, only 2 N image stacks will be used for further micro and macro structural analysis. The data collected from the 7 N scan (along with the 2 N scan) will be used in the future to determine the internal three-dimensional bone strain as described in Chapter 7.

3.5 Micro and Macro Structural Analysis

Custom MATLAB code was developed to quantify different micro and macro structural properties of the femoral neck image stacks. The projection images obtained from the CT

scanner were reconstructed into TIFF images (Fig. 3.8A). These images were binarized and removed of non-bone (artefacts, gauze, and noise) objects (Fig. 3.8B). The image stacks were resliced to measure the femoral neck angle in the orthogonal views, XZ and YZ (Fig. 3.8C). The orthogonal views were rotated to align the horizontal axis and vertical axis to the femoral neck axis in the YZ and XZ view, respectively (Fig. 3.8D). Now aligned, the beginning of the and ending of the femoral neck were determined with the femoral head side denoted as the end. The image stack was resliced to its original XY configuration and slices of interest were identified (Fig. 3.8E). Slices of interest were the first slice of the femoral neck (0%) and sequential slices along the femoral neck length in 10% intervals up to the last slice of the femoral neck (100%). The femoral neck was isolated in the slices of interest and the structural properties were measured. The cortical area was determined by measuring the amount of bone in each slice of interest (Fig. 3.8F). The cross sectional area was determined by measuring the area within the outer boundary of the femoral neck (Fig. 3.8G). The cortical fraction was calculated by taking the ratio of cortical area over the cross sectional area. The major and minor diameters of the femoral neck were determined by using an ellipse to model the femoral neck bone (Fig. 3.8H). The cortical thickness was calculated by modeling the inner hollow of the femoral neck as an ellipse and then taking the mean of differences between the major and minor diameters of the two ellipse models.

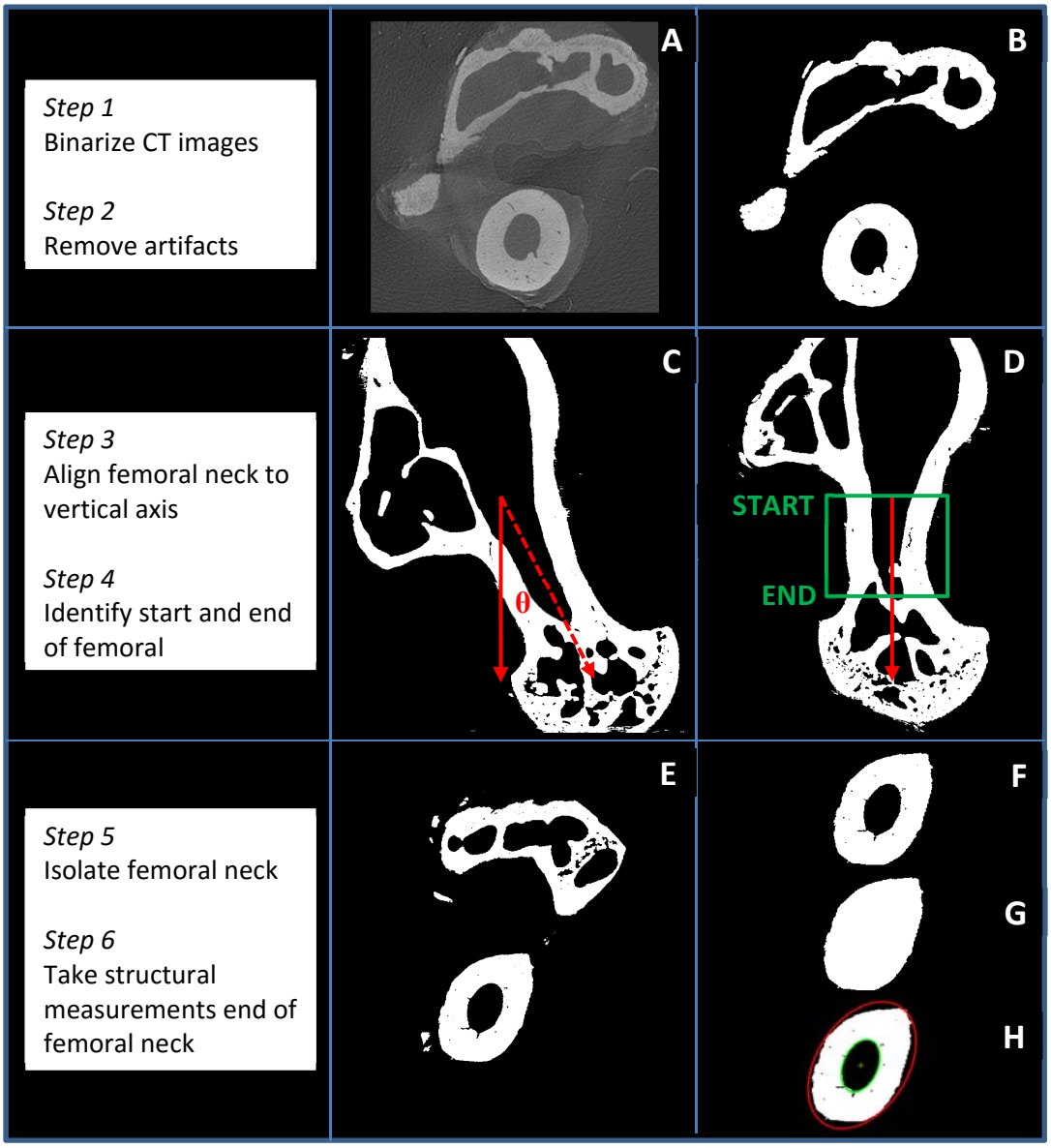

Figure 3.8: The breakdown of how the micro and macro structural parameters were determined. (A) The original image stack was (B) binarized and removed of any non-bone items. (C) The image stack was resliced into an orthogonal view to measure the angle offset of the vertical axis with the femoral neck axis. (D) The orthogonal slice was rotated to align the femoral neck axis and the vertical axis. The beginning and ending of the neck were also identified. (E) The orthogonal view was resliced to the original XY configuration. (F) Once the femoral neck bone was isolated, the cortical area was measured. (G) The cross sectional area can be measured from the area within the outer boundary of the femoral neck. (H) Ellipses modeled the geometry of the femoral neck bone and the inner hollow. From these models, the major diameter, minor diameter and cortical thickness can be measured.

CHAPTER 4: RESULTS

4.1 Mechanical Testing

The mean peak load of the specimens was 18.25 ± 3.05 N (range = 14.74 – 24.37 N) (Table 4.1). While the peak load was fairly consistent, the stiffness of each specimen was more variable with a mean of 81.13 ± 47.61 N/mm (range = 29.92 – 149.65 N/mm). The force – displacement behavior of specimens 1 – 4 exhibited sudden drops in force as displacement increased (Fig. 4.1), while the stiffness of .specimens 5 – 10 was smooth. The displacements at peak load of specimens 1 – 4 and specimens 5 – 10 were 0.563 ± 0.068 mm and 0.304 ± 0.041 mm, respectively ($p < 0.01$). The mean displacement at ultimate load for all specimens was 0.41 ± 0.14 mm. In all specimens, fracture occurred in the femoral neck.

Table 4.1: Femur Macro-geometric and Mechanical Properties

Specimen	Measurements						
	Potted Length (mm)	Side Angle (deg)	Back Angle (deg)	Displacement (mm)	Strain (με)	Stiffness (N/mm)	Peak Load (N)
1	6.28	76.20	87.38	0.587	93520	33.18	18.78
2	7.51	75.11	76.52	0.461	61403	46.21	16.16
3	8.17	67.62	67.22	0.605	73990	36.50	14.74
4	8.34	67.84	73.86	0.598	71777	29.92	17.31
5	5.42	77.84	71.57	0.352	65013	87.37	24.37
6	6.08	88.95	72.82	0.263	43222	108.74	22.56
7	6.05	110.42	61.99	0.314	51898	149.65	16.38
8	6.70	79.93	85.84	0.245	36575	140.10	18.63
9	5.76	68.60	90.34	0.322	55942	129.44	17.71
10	5.87	73.87	99.20	0.328	55835	50.19	15.84

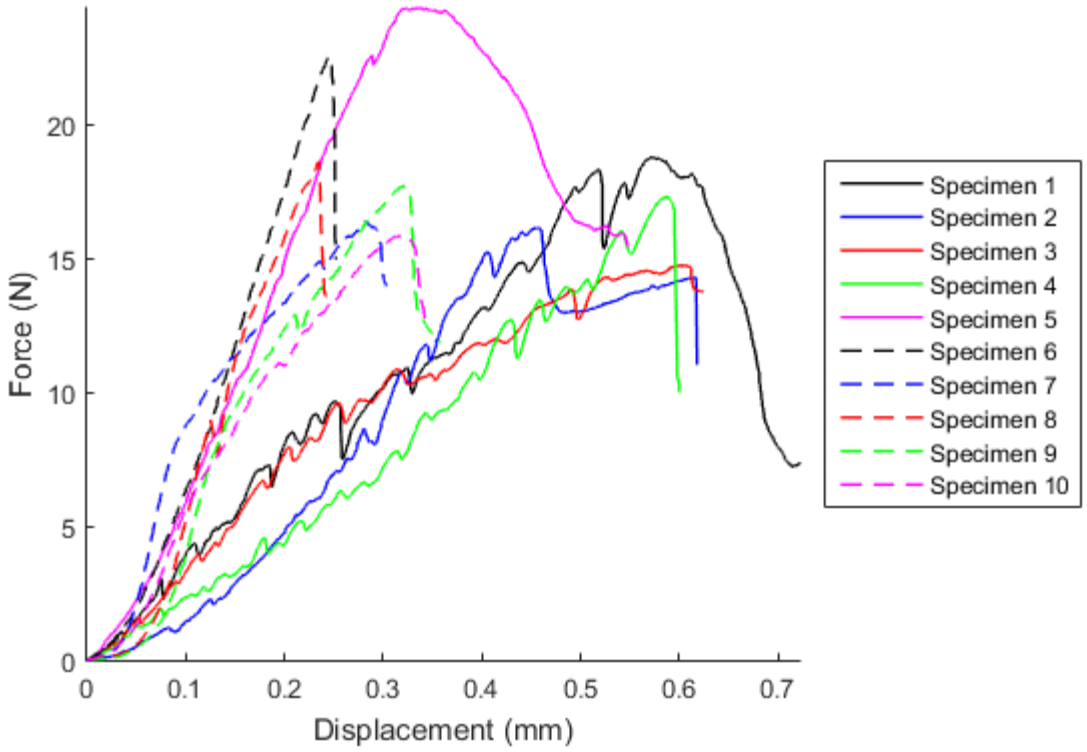

Figure 4.1: The force – displacement relationship of murine femurs tested to failure. The average stiffness was 81.13 ± 47.61 N/mm and femoral neck peak load was 18.25 ± 3.05 N.

Most femurs were potted within ± 12° of the two horizontal axes with an average side angel of 78.36 ± 12.90 ° and a back angle of 78.67 ± 11.58 °. The manual positioning of the femur did not have an influence on the measured ultimate load between specimens. There was no significant correlation between the peak load and the side angle or back angle (Fig. 4.2).

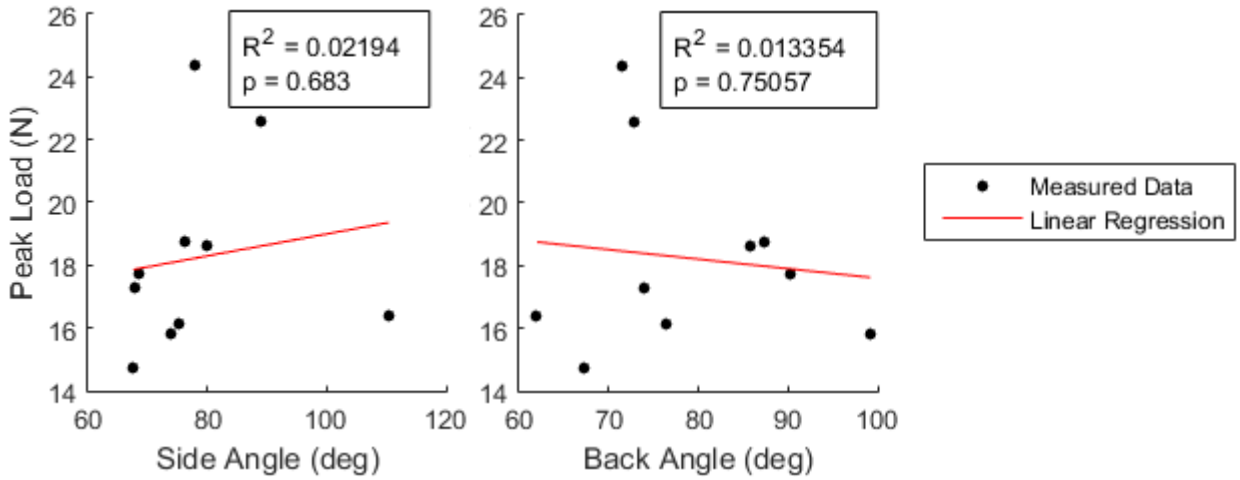

Figure 4.2: The correlation between femoral peak load and side angle or back angle lacked any statistical significance ($p > 0.1$).

4.2 Structural Analysis

The measured structural variables (major diameter, minor diameter, cortical thickness, cross sectional area, cortical area, and cortical fraction) varied along the length of the femoral neck. The beginning of the neck, closest to the femur shaft, was denoted as the 0% position. The end of the neck, closest to the femoral neck , was denoted as the 100% positions.

The major diameter of the femoral neck followed a concave curve with the average largest major diameter (1.18 ± 0.07 mm) at the beginning (0% position) and end of the neck (100% position) for all specimens (Fig. 4.3). The average minimum major diameter (0.95 ± 0.06 mm) was 19.9% smaller than the largest average diameter and located between 40% and 70% along the femoral neck for all specimens. The majority of specimens had the smallest major diameter located at 50%.

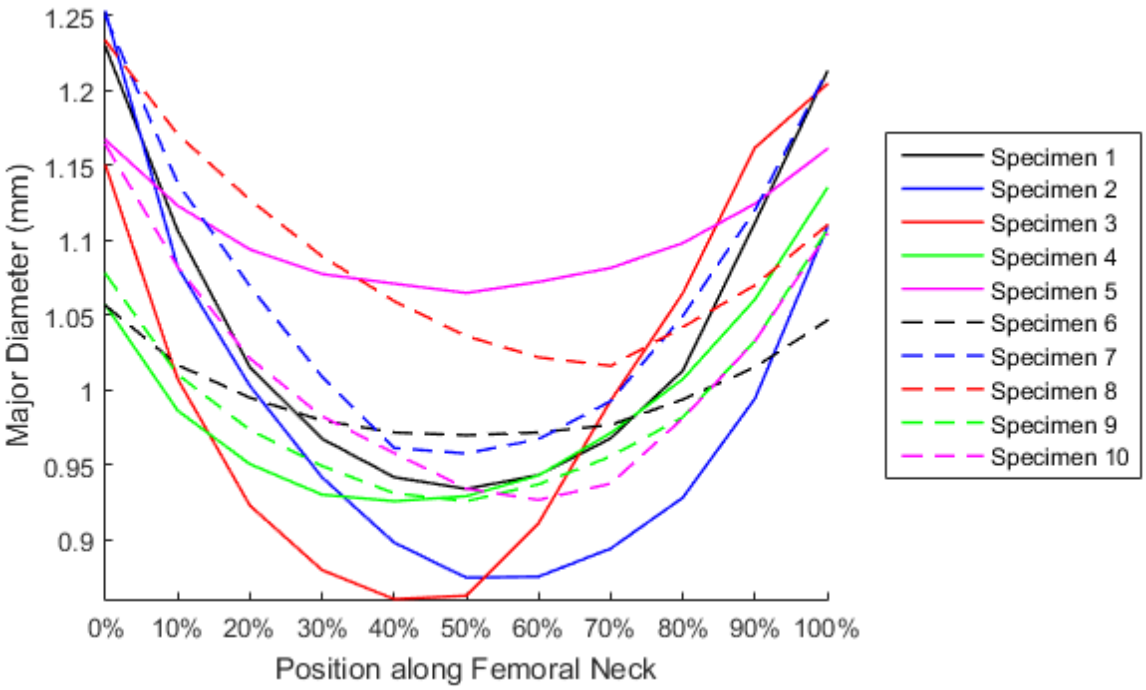

Figure 4.3: The major diameter as a function of position along the femoral neck. The major diameter is highest at 0% and 100% along the femoral neck with the lowest major diameter falling at or between 40% and 70%.

The minor diameter was constant between 0% and 70% of the femoral neck with an average value of 0.69 ± 0.05 mm. After 70% along the femoral neck the minor diameter began to increase in magnitude (Fig. 4.4). The maximum minor diameter was found at the end of the femoral neck (100% position) for all specimens. The average maximum minor diameter (0.81 ± 0.08 mm) was 17.2% larger than the average value from 0% – 70%.

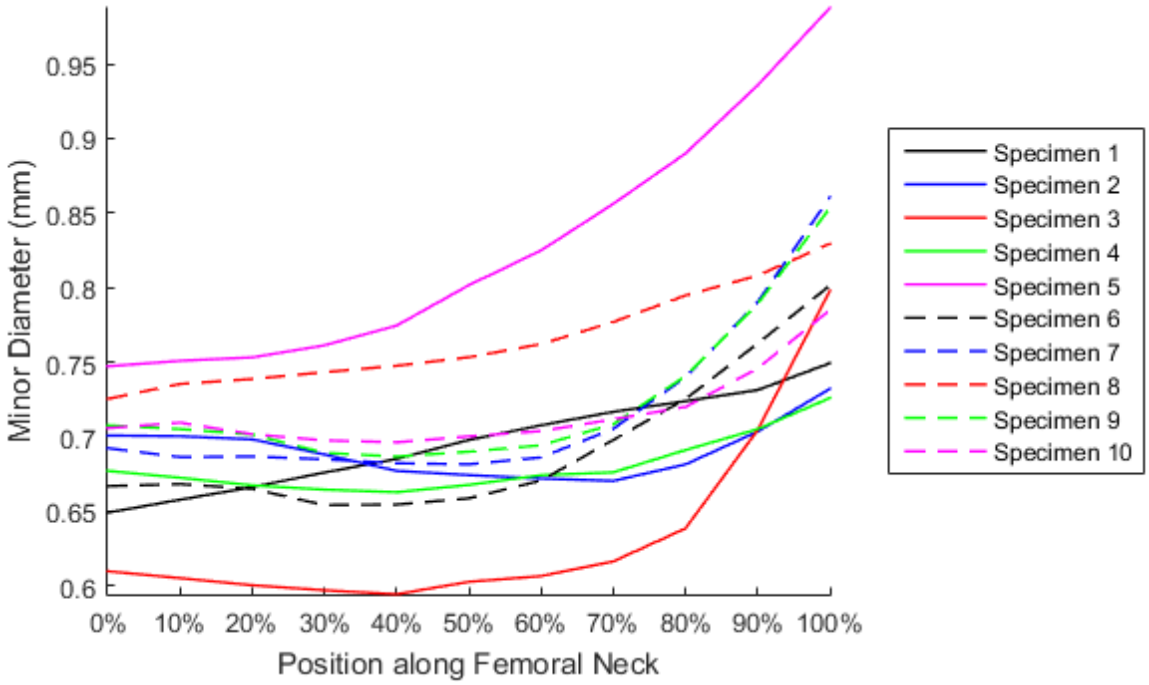

Figure 4.4: The minor diameter as a function of position along the femoral neck. The minor diameter is highest at 100% along the femoral neck with the lowest major diameter falling at or between 0% and 70%.

Cortical thickness was highest at the beginning of the neck and gradually decreased as it approached the end of the neck (Fig. 4.5). The maximum cortical thickness was located within 10% of the beginning of the neck for nine of the specimens tested. The minimum cortical thickness was located within the last 40% of the end of the neck. The average cortical thickness decreased by 29%, from 0.27 ± 0.04 mm to 0.19 ± 0.02 mm.

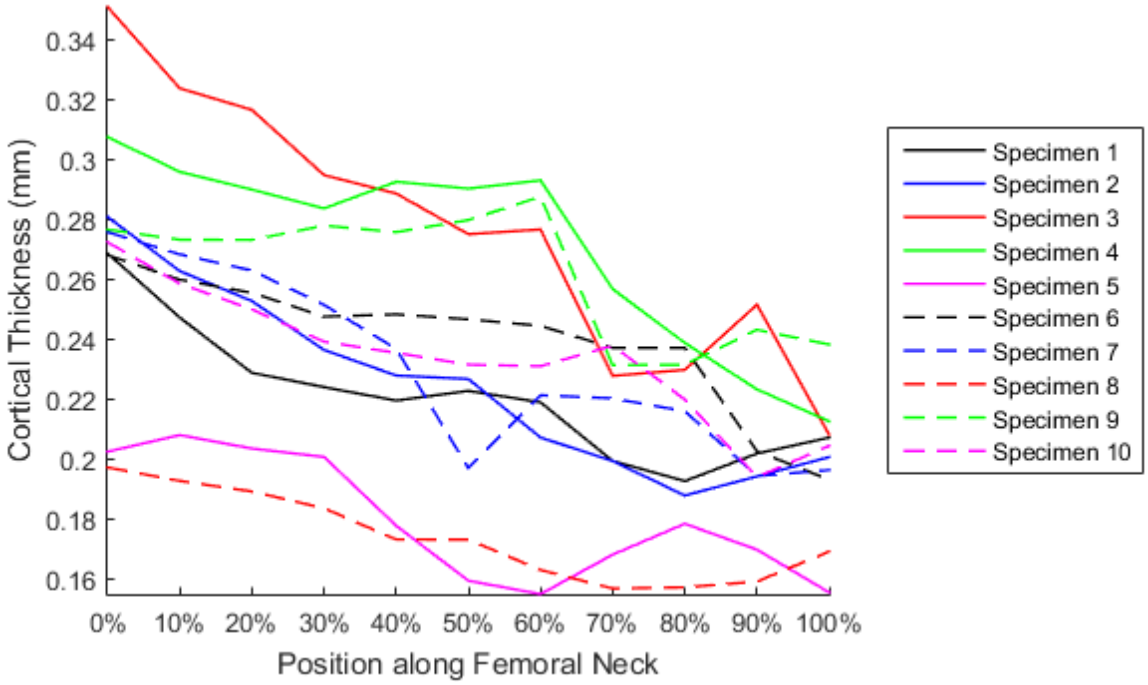

Figure 4.5: The cortical thickness as a function of position along the femoral neck.

Cross sectional area initially decreased but then curved upwards towards the end of the neck (Fig. 4.6). The maximum cross sectional area was highest at the end of the neck (100% position) for nine of the specimens tested with an average value of 0.72 ± 0.08 mm^2. The average maximum cross sectional area was 41.4% higher than the average minimum cross sectional area of 0.51 ± 0.07 mm^2. The minimum cross sectional area was between 30% and 40% with the majority of specimens having the lowest cross sectional area at 40%.

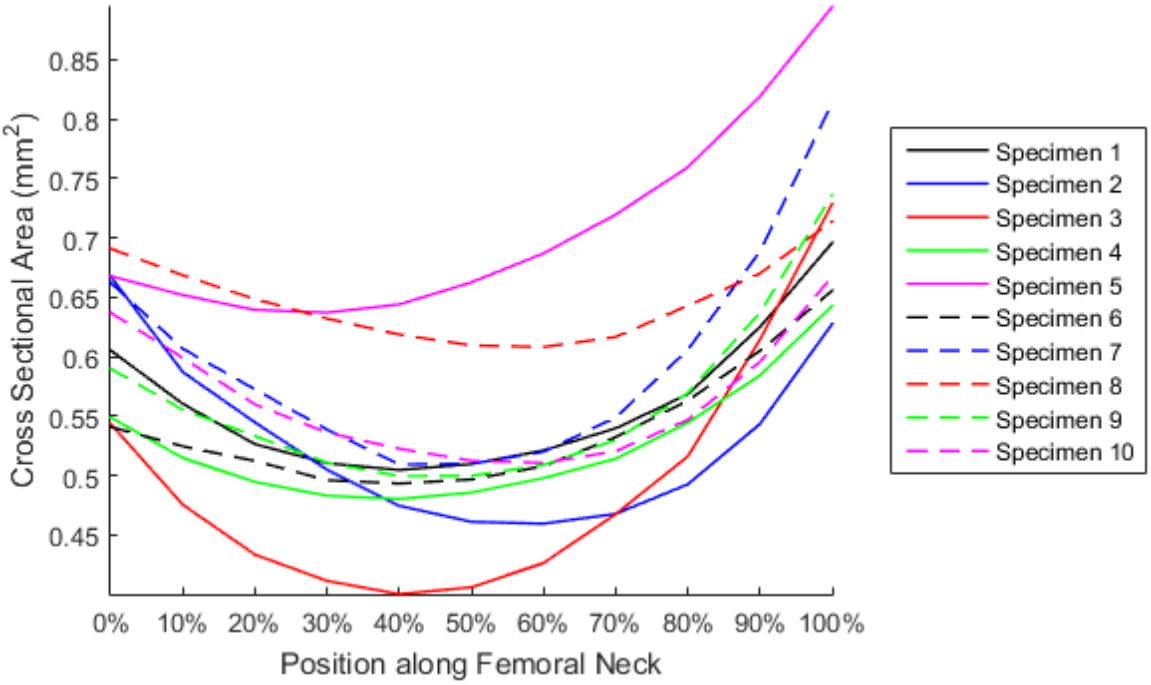

Figure 4.6: The cross sectional area as a function of position along the femoral neck. The cross sectional area is highest at 100% along the femoral neck with the lowest cross sectional area falling at or between 30% and 40%.

As expected, the cortical area had a similar curve a similar trend as major diameter (Fig. 4.7). The cortical area of the femoral neck followed a concave curve with the largest area at the beginning (0% position) and end of the neck (100% position) for all specimens. The minimum cortical area was between 40% and 50% along the length of the femoral neck for the majority of specimens. The average maximum and minimum cortical areas were 0.55 ± 0.05 mm^2 and 0.42 ± 0.03 mm^2, respectively. The average maximum cortical area was 31.2% higher than the average minimum.

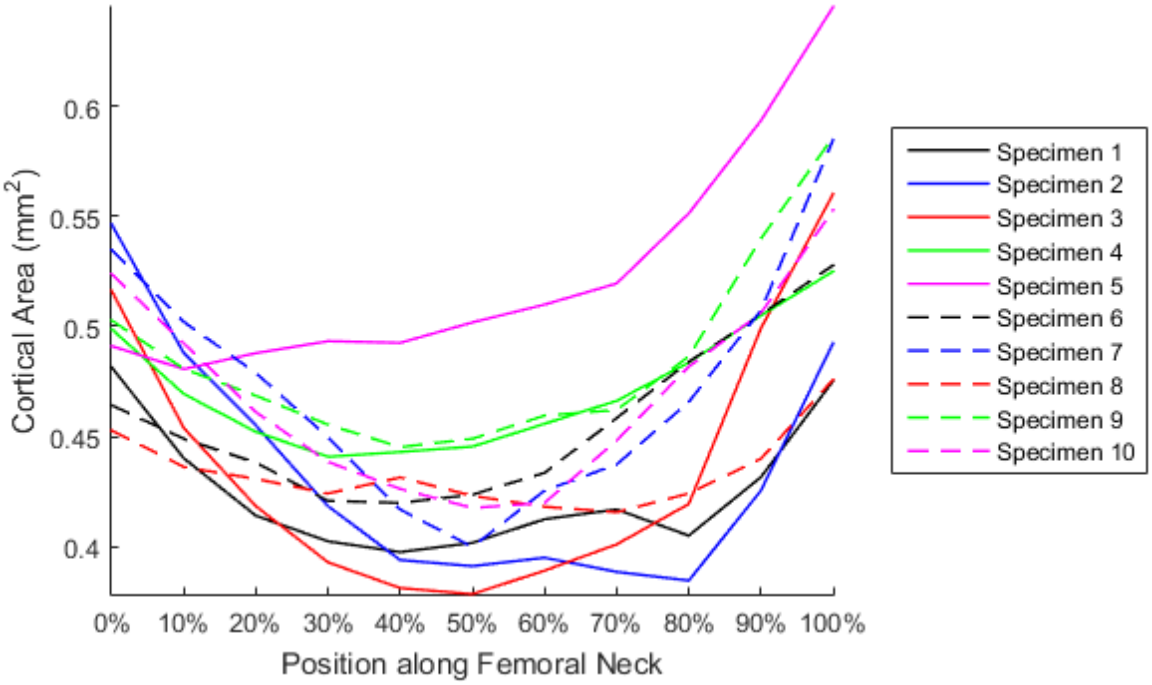

Figure 4.7: The cortical area as a function of position along the femoral neck. The cortical area is highest at 0% and 100% along the femoral neck with the lowest major diameter falling at 40% or 50% for the majority of specimens.

Finally, cortical fraction was approximately constant throughout the beginning of the neck (between 0% and 80% along the length) before declining towards the end (Fig. 4.8). The average constant cortical fraction was 0.82 ± 0.07 and decreased by 8.2% to the average minimum cortical fraction of 0.76 ± 0.06. The minimum cortical fraction was located at the end of the femoral neck (100% position) for the majority of specimens.

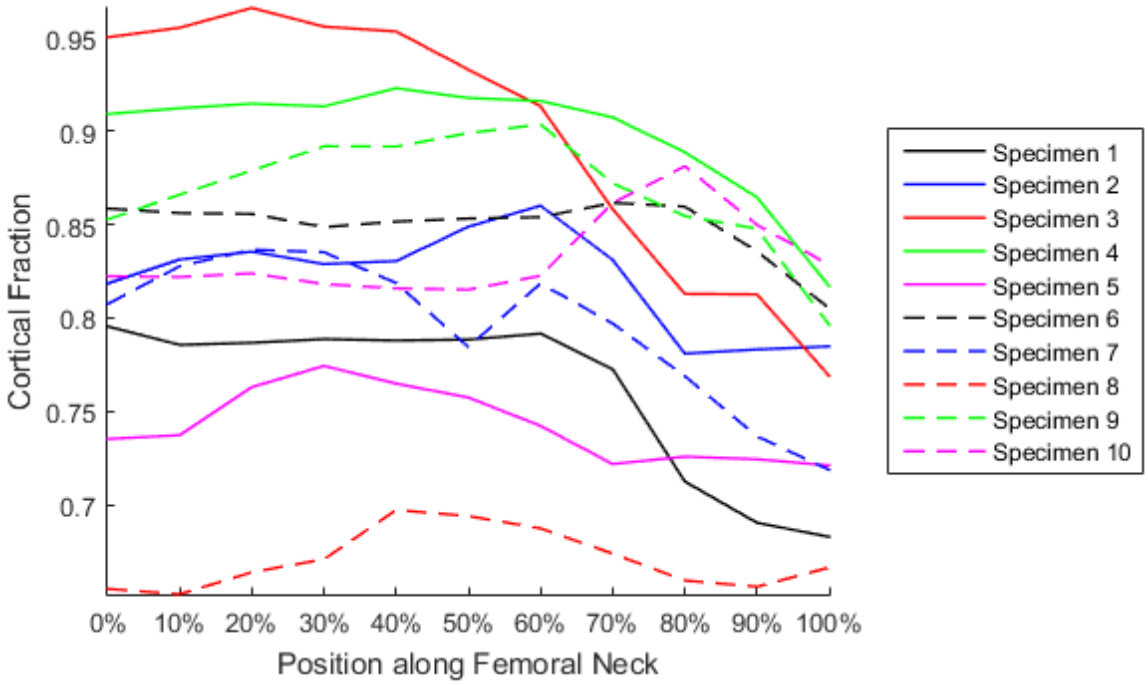

Figure 4.8: The cortical fraction as a function of position along the femoral neck. The cortical fraction diameter is highest at within 80% of the beginning of the femoral neck with the lowest major diameter falling at 100% for the majority of specimens.

For raw specimen data associated with Fig. 4.3 – Fig. 4.8, please see Appendix B.

4.3 Correlating Structure to Peak Load

Femoral ultimate load could be partially explained by all structural variables with the exception of cortical fraction. However, the correlation between structure and load was spatially variable (Table 4.2). Major diameter (R^2 = 0.6048), minor diameter (R^2 = 0.5871), cross sectional area (R^2 = 0.5876), and cortical area (R^2 = 0.5401) had a positive linear correlation , while cortical thickness (R^2 = 0.4376) exhibited a negative linear correlation (Fig. 4.9 – Fig. 4.13). The coefficient of determination (R^2) of the variables ranged from 0.4376 (cortical thickness) to 0.6048 (major diameter).

Table 4.2: Single Variable Linear Regression Results

	Variables											
	Major Diameter		Minor Diameter		Cortical Thickness		Cross Sectional Area		Cortical Area		Cortical Fraction	
Position	R^2	*p*	R^2	*p*	R^2	*p*	R^2	*p*	R^2	*p*	R^2	*p*
0%	0.061	0.490	0.182	0.219	0.438	***p* < 0.05**	0.004	0.858	0.388	***p* < 0.1**	0.178	0.224
10%	0.030	0.633	0.211	0.181	0.370	***p* < 0.1**	0.111	0.346	0.059	0.498	0.203	0.191
20%	0.186	0.214	0.241	0.149	0.340	***p* < 0.1**	0.219	0.173	0.057	0.508	0.182	0.219
30%	0.363	***p* < 0.1**	0.264	0.129	0.267	0.127	0.312	***p* < 0.1**	0.261	0.131	0.160	0.252
40%	0.516	***p* < 0.05**	0.328	***p* < 0.1**	0.261	0.131	0.422	***p* < 0.05**	0.447	***p* < 0.05**	0.177	0.226
50%	0.593	***p* < 0.01**	0.396	***p* < 0.1**	0.213	0.180	0.502	***p* < 0.05**	0.540	***p* < 0.05**	0.154	0.261
60%	0.605	***p* < 0.01**	0.466	***p* < 0.05**	0.225	0.166	0.559	***p* < 0.05**	0.515	***p* < 0.05**	0.210	0.184
70%	0.393	***p* < 0.1**	0.557	***p* < 0.05**	0.156	0.259	0.588	***p* < 0.01**	0.493	***p* < 0.05**	0.167	0.241
80%	0.126	0.315	0.587	***p* < 0.01**	0.069	0.464	0.538	***p* < 0.05**	0.361	***p* < 0.1**	0.066	0.472
90%	0.000	0.971	0.536	***p* < 0.05**	0.222	0.169	0.396	***p* < 0.1**	0.204	0.190	0.066	0.475
100%	0.080	0.428	0.347	***p* < 0.1**	0.358	***p* < 0.1**	0.177	0.226	0.085	0.414	0.053	0.522

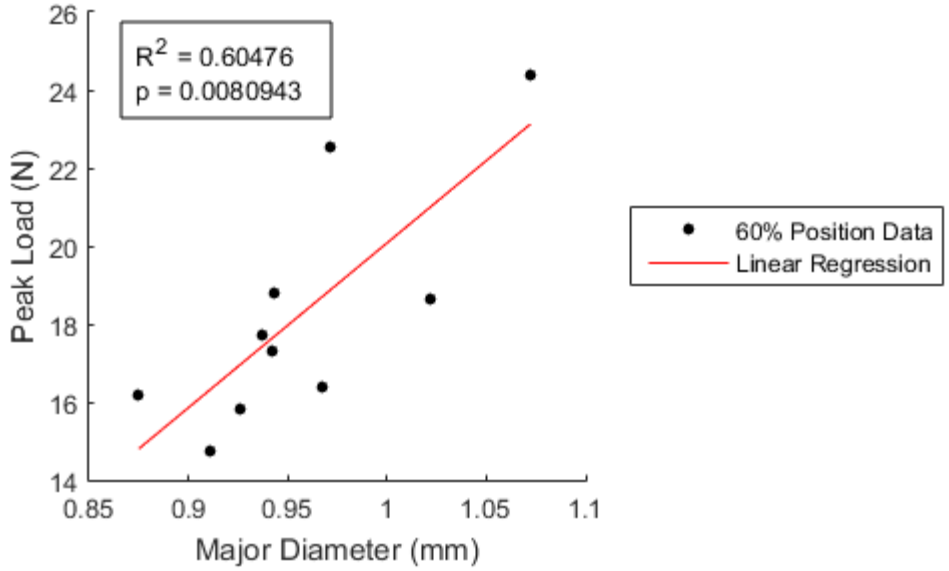

Figure 4.9: The major diameter had significant correlations ($p < 0.05$) at the center of the femoral neck, from 40% to 60%. The highest R^2 was located at 60% along the femoral neck with a value of 0.60476.

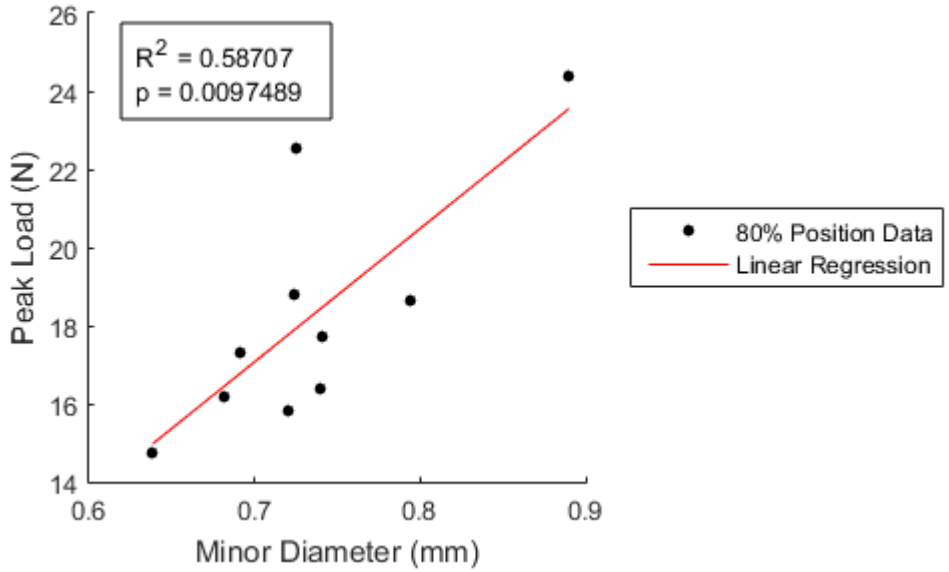

Figure 4.10: The minor diameter had significant correlations ($p < 0.05$) from 60% to 90% along the femoral neck. The highest R^2 was located at 80% along the femoral neck with a value of 0.58707.

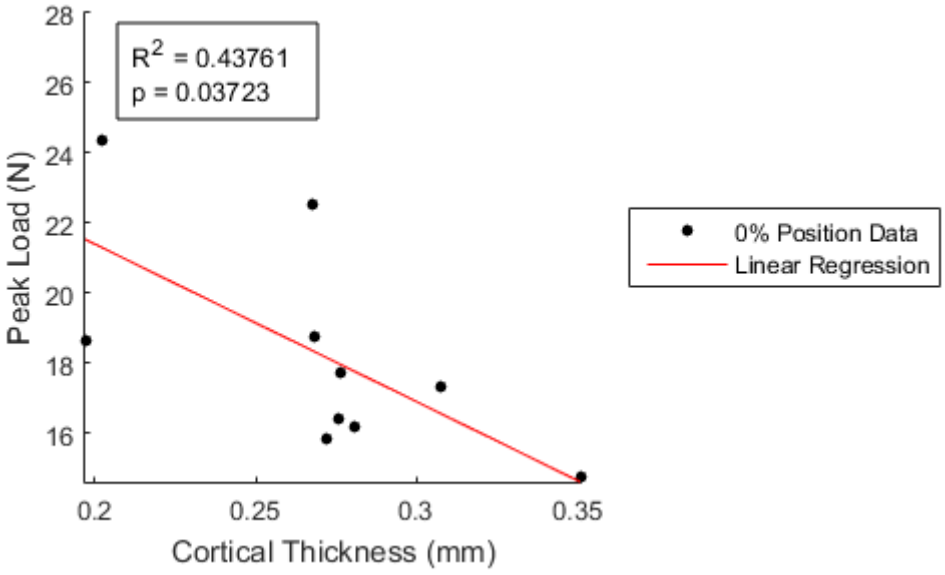

Figure 4.11: Cortical thickness had significant correlations ($p < 0.05$) at the beginning of the femoral neck. The highest R^2 was located at 0% along the femoral neck with a value of 0.43761.

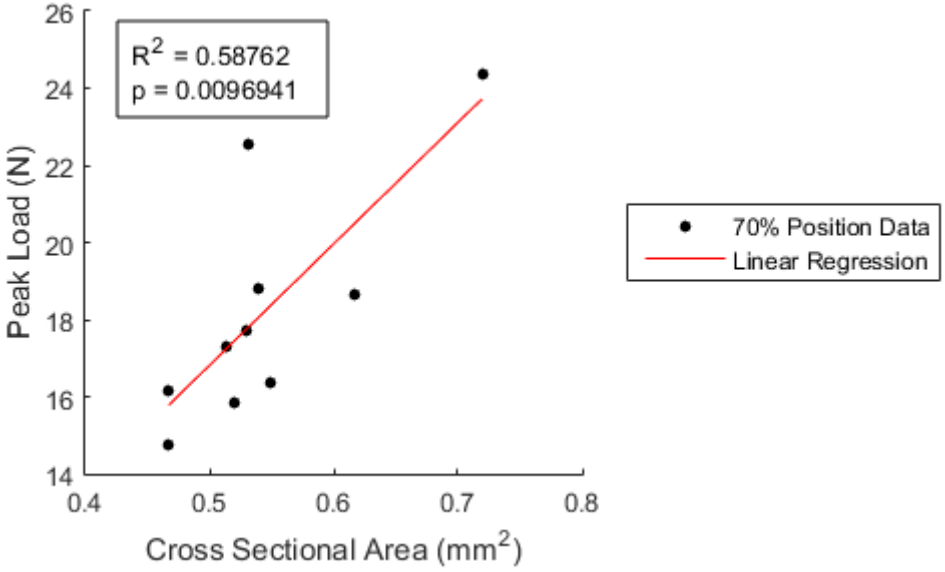

Figure 4.12: Cross sectional area had significant correlations ($p < 0.05$) from 40% to 80%. The highest R^2 was located at 70% along the femoral neck with a value of 0.58762.

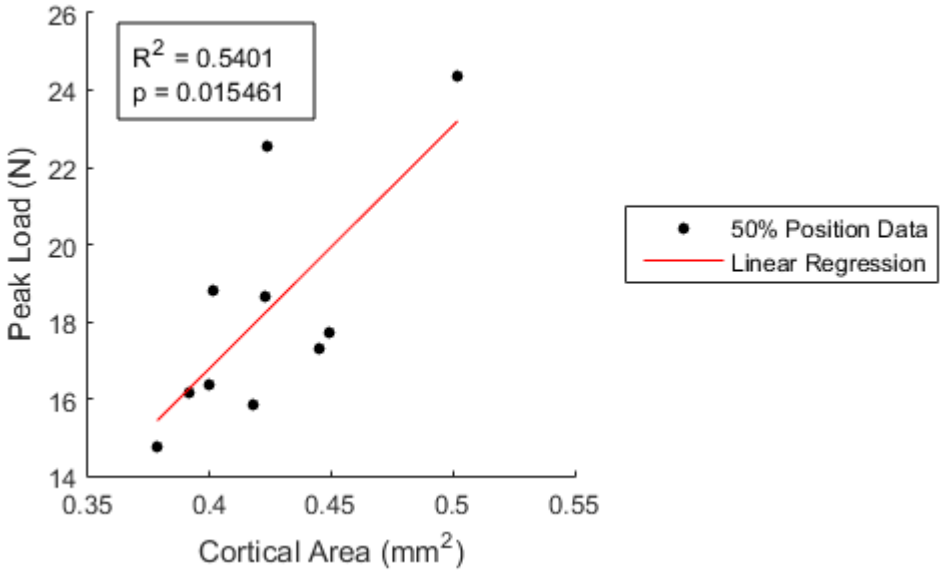

Figure 4.13: Cortical area had significant correlations ($p < 0.05$) from 40% to 70%. The highest R^2 was located at 50% along the femoral neck with a value of 0.5401.

When performing linear multivariable regressions, only two structural variables resulted in significant correlation with ultimate load ($p < 0.05$). The highest significant R squared value was obtained using major diameter and cortical area ($R^2 = 0.6642$) as inputs (Fig. 4.14). The regression coefficients of major diameter and cortical area were 1.57 and 1.10, respectively (with a constant of 18.25).

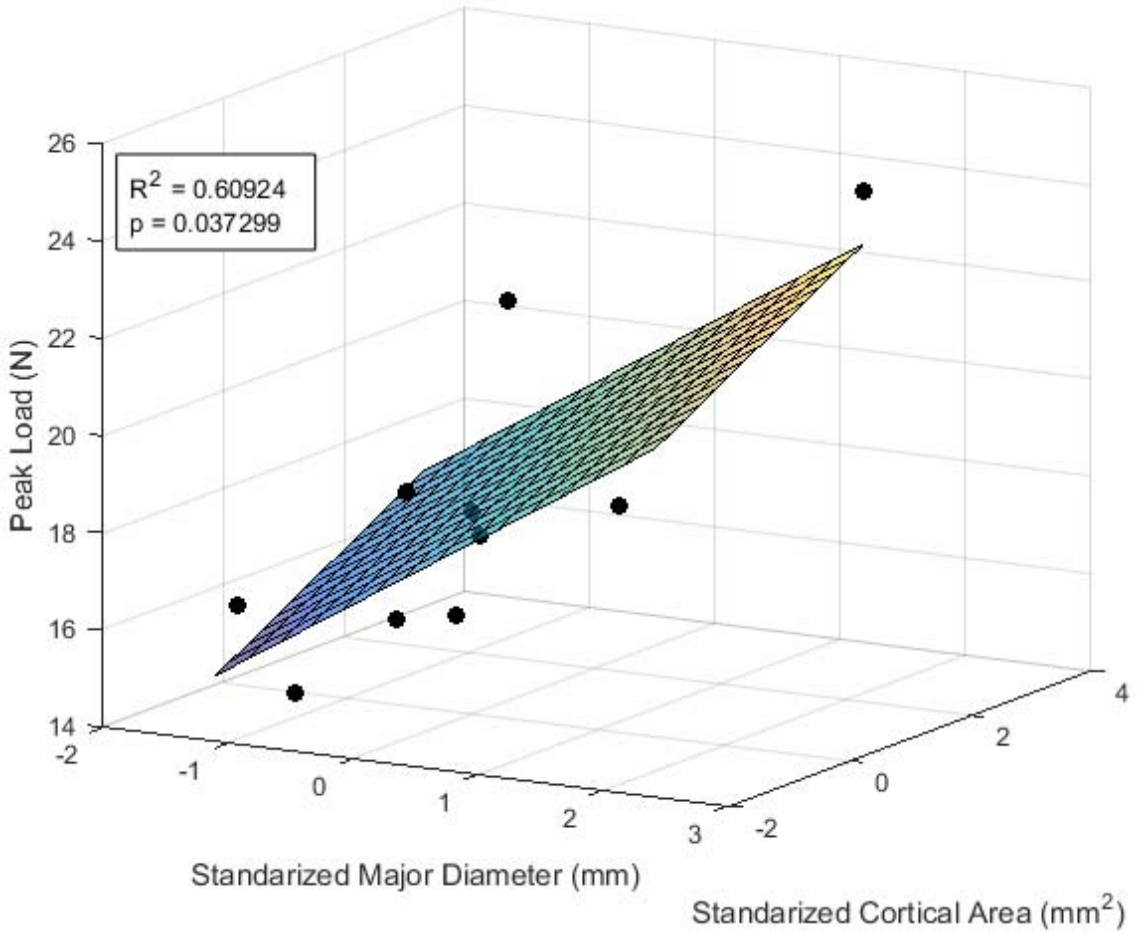

Figure 4.14: Surface plot of a two variable regression analysis using the standardized major diameter and cortical area as inputs. These variables yielded the highest R squared correlation that was significant.

CHAPTER 5: DISCUSSION

Hip fractures, especially at the femur, can lead to increased levels of mortality and morbidity (Sernbo and Johnell). Identifying the structural variables that correlate with the peak load of the femoral neck provides a powerful non-invasive means for predicting those at risk of fracture without causing mechanical damage to the bone.

The measured peak load of the femurs in this study (18.25 ± 3.05 N) closely resemble the peak load measured by other studies. Jamsa found the peak load of the femoral neck to be 18.6 ± 4.1 N and 18.9 ±3.5 N in successive studies (Jämsä, Tuukkanen, and Jalovaara; Jämsä et al.). The stiffness (81.13 ± 47.61 N/mm) of the specimens was within the range of the studies performed by others. Turner reported the stiffness of murine femurs with low and high bone mineral densities (BMD) as 90 ± 5 N/mm and 118 ± 3 N/mm, respectively (Turner et al.). Voide also reported stiffness of murine femurs with low and high bone mineral densities but as 51.2 ± 6.9 N/mm and 89.7 ± 9.2 N/mm, respectively (Voide, Van Lenthe, and Müller). While the mean stiffness is comparable to the values reported by these studies, the large standard deviation in our study may be influenced by variation of bone mineral density but this remains to be evaluated.

The structural variables, cross sectional area and cortical thickness, were measured at specific positions along the femoral neck. However, for comparison to other studies, these values were averaged together for all specimens. Jamsa has reported the cross sectional area of the femoral neck as 0.67 ± 0.15 mm^2 and 0.86 ± 0.17 mm^2 in successive studies (Jämsä, Tuukkanen, and Jalovaara; Jämsä et al.). Voide reported the cross sectional area as 0.58 ± 0.03 mm^2 for low BMD femurs and 0.66 ± 0.06 mm^2 for high BMD femurs (Voide, Van Lenthe, and Müller). This study had an average cross sectional area of 0.57 ± 0.06 mm^2 which was similar to the low BMD value reported by Voide; but with the standard deviation, our study overlaps with the high BMD femurs and with Jamsa's first study. The average cortical thickness of the tested specimens was 0.23 ± 0.02 mm similar to the cortical thickness of low BMD specimens of Turner (0.294 ± 0.005 mm) and Voide (0.24 ± 0.02 mm) (Turner et al.; Voide, Van Lenthe, and Müller). It should be noted that the cortical thickness of this study was approximated using a simplified

ellipse while the other studies used direct 3D morphometry (Turner) and a thickness algorithm (Viode).

The failure mode of the femoral neck peak load suggests that bending may have contributed to the fracture. Investigating the bone after testing showed that the fracture occurred in the femoral neck, with little visible damage to the femoral head. The anticipated bending forces due to the testing setup were deemed acceptable because physiological loading of the murine femur induces bending on the neck as well. Of greater concern was the consistency of the bending forces within the test group. Because bending forces were not directly measured, the back and side angle of the femoral neck were used as guides to limit the variation in bending forces. However, neither angle was significantly correlated with the peak load (see Chapter 4).

The peak load of the mouse femur can be determined by measuring specific structural variables at certain areas along the femoral neck. Major diameter, minor diameter, cross sectional area, and cortical area had significant positions located at or between 40% and 90% along the femoral neck, while cortical thickness had significance at 0%. The major diameter had significant correlations between 40% and 60%, which is also where the major diameter was the smallest. Observing Fig. 4.9, major diameter size is positively correlated to peak load, so the smaller the major diameter is in this range, the less load the bone can withstand.

Minor diameter had significant correlations between 60% and 90%. The minor diameter begins to increase near the end of the femur with the maximum value found at 100% along the femoral neck, while the minimum can be found from 0% to 70%. However, the variability in the minimum minor diameter size in the first half of the femoral neck likely prevented any single position within the distal neck from being more significant. Therefore, the only significant correlations could be determined towards the end of the femoral neck, excluding the 100% location. The minor diameter did not follow the same trend as the as the major diameter. Our results confirm that the femoral neck is elliptical in nature. The eccentricity of the proposed ellipse decreases (major diameter decreases, minor diameter is constant) along the femoral neck until approximately 50% - 60%. The eccentricity continues to decrease (major diameter greatly

increase, minor diameter increases), but at a slower rate, as the neck develops into a more circular cross section (Fig. 5.1).

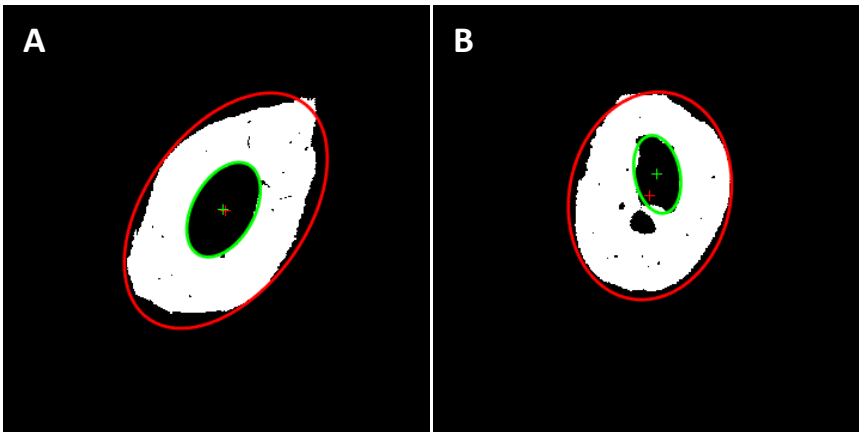

Figure 5.1: (A) At the beginning of the neck, the ellipse has a high eccentricity. (B) A 70% along the neck, the eccentricity has decreased from earlier in the femoral neck.

This suggests that the femur starts as an ellipse and gradually becomes more circular as it transitions into the femoral head. This highly elliptical structure at the start of the neck could be purposely designed to counter the high physiological bending loads seen at the base of the femoral neck as well as provide a smooth integration into the greater trochanter.

The cross sectional area between 40% and 80% were significantly correlated with peak load. The minimum of the cross sectional area curve for the majority of the specimens was located at 40%. The cross sectional area is related to the major and minor diameter of the specimen. When these two variables are at the largest then the cross sectional area will also be at its maximum value. The maximum cross sectional area is found at 100%, the same location of the maximum values for major and minor diameter.

Cortical area between 40% and 70% along the femoral neck was also significantly correlated to peak load, with the minimum cortical area for the majority of specimens found at 40% - 50%. One could expect this minimum area to be further along the neck, similar to the behavior of cortical thickness because there is less bone material. However, the major diameter increased during the last 50% along the length, which seems to counter act the decreased thickness.

Unlike the other variables, cortical thickness was only significant and best correlated at the 0% position. This is where the bone is most likely to see the highest bending, so it is not surprising that this position is important in determining the peak load of the femoral neck.

Kersh investigated the change of structure along the length human femurs. The cross sectional area, cortical fraction, and cortical thickness of the murine necks in this study had the same trends as those of human femurs (Kersh et al.). Measurements of cortical area were included in both studies, however, in our study cortical area shows a quadratic relationship with position, while Kersh reported a negative linear relationship. We also observed that the internal structure of the bone near the end of the neck began to have connecting branches across the hollow neck. These branches can be classified as trabecular bone, yet was included in the cortical area measurements. This may cause a slight overestimation of the cortical bone area near the end of the femoral neck.

Several significant correlations were found between individual variables and the peak load of the femoral neck. Furthermore, a two variable correlation was found that yielded the highest R^2 of 0.664. Therefore, 67% of the variation in femoral neck peak load can be explained by measuring the major diameter and cortical area at the highest correlation positions (60% and 50%). However, position was not sensitive and correlations can be taken at specific locations and still achieve a high correlation to peak load (Table 5.1). The dark gray area indicates a significance of $p < 0.05$ and light gray has a slightly weaker significance of $p < 0.1$. For single correlations, individual variables can be measured within their significance range without a significant decrease in R^2 values.

Table 5.1: Number of Significant Variables at Each Position along Femoral Neck

	$p < 0.05$	$p < 0.01$	Total Variables Significant
0% Position	1	0	1
10% Position	0	0	0
20% Position	0	0	0
30% Position	3	0	3
40% Position	3	1	4
50% Position	4	1	5
60% Position	3	1	4
70% Position	2	1	3
80% Position	1	0	1
90% Position	0	0	0
100% Position	0	0	0

Using a computational model, Kersh found that the cortical thickness and cortical area had the highest single variable correlations with peak load ($R^2 = 0.59$ and $R^2 = 0.49$, respectively), while in this study(using experimental methods) we found that the highest correlations to peak load were associated with major diameter and cross sectional area ($R^2 = 0.605$ and $R^2 = 0.588$, respectively) (Kersh et al.). This difference could be a result of the different specimens, differences between computational and experimental work, or how the parameters were measured.

Knowing which structural variables to investigate to determine the peak load of the bone allows for future research to predict the peak load without having to mechanically test the bone. This information will be useful for those researchers studying mice, especially those performing in vivo studies, which make it impossible to mechanically test the femur until end point analyses. These results could be extracted to human specimens, but further experiments will be necessary to check the validity of the proposed structural relationships to peak load.

CHAPTER 6: LIMITATIONS

This study has several limitations. The murine femurs were analyzed under loads that were not based on physiological conditions. The Deben testing stage manual states that it has a resolution of ± 5 N, however, we did not quantify what effect the manufacturer resolution had on our measurements. In addition, the load cell of the Deben testing stage had a slight force drift, which was seen when performing initial tests on the aluminum fixture. This drift may contribute to some of the decrease in force seen in the step mechanical tests (Fig. 3.7).

The specimens were wrapped in PBS soaked gauze for the duration of testing, however, after almost 5 and half hours of scanning, the specimens may have started drying out leading to degradation. Drying could be caused by the ambient air inside the testing stage or by the constant ionizing radiation bombarding the specimen.

A limitation of the analysis was the modeling of the femoral neck and internal hollow cavity as ellipses. This simplification of the geometry was used to calculate the major diameter a minor diameter, and the cortical thickness. While some regions of the femoral neck could be well characterized by an ellipse, other regions deviated from this idealized geometry. In addition, towards the end of the femoral neck, bone began to branch across the neck. The branches and increase number of pore suggest that some trabecular bone was present in the ending slices, yet all of the bone was included in the measuring of cortical area.

The delay in testing to failure for a subset of our specimens may have impacted the stiffness measurements we calculated. Specimen 1 to 4 underwent a step mechanical test as explained in Chapter 3 and then was stored between 20 to 30 days before being tested to failure, while the remaining specimens were scanned and tested immediately with no delay. When comparing these specimen groups (delayed and immediate), there was no significance difference between peak load of the groups, but there was a significant difference in stiffness ($p < 0.01$). For this reason, our mechanical analysis was limited to the peak load of bones. The delayed specimens may have been stored for too long causing degradation . However, the specimens tested

immediately after scanning could have become dehydrated by the scanning process, which could explain the decrease in deformation before fracture (Fig. 4.1). The delayed specimen group had more intermediate failure points along the force-displacement curve as it approached peak force. However, the stiffness of these specimens was lower and the deformation was higher, suggesting the bone was more ductile as damage occurred in response to the higher strain levels. Potential solutions to avoid these issues in future experiments are discussed in Chapter 7.

Lastly, this study was done on murine specimens, so any comparisons to other animal species or humans must be carefully considered.

CHAPTER 7: FUTURE WORK

7.1 Improvements on Current Methods

The aluminum base fixture was assumed to be rigid and have no contribution to the results. The base fixture underwent initial testing resulting in consistent stiffness measurements under high loads, but the custom fixture with its unique geometry still needs to be further validated to ensure the fixture itself shares no load during testing. The load cell drift discussed in Chapter 6 needs to be further validated to determine if it is contributing to the force decrease seen in the mechanical tests.

In addition, it may be advantageous to perform the testing in an aqueous solution to ensure bone hydration. Most importantly, all testing must be done as consistently as possible to avoid unintentional variances in the test specimens.

7.2 Digital Volume Correlation (DVC)

As discussed in Chapter 2, DVC is a volume correlation technique that allows for the calculation of local three-dimensional strain within the bone. Using DVC in conjunction with this study will allow for the correlation of different macro and micro structural parameters to local areas of bone mechanics. This has never been applied to whole murine femur bones, and will be the next steps following this study.

Before beginning the analysis of the data collected in this study, the DVC software, Vic Volume by Correlated Solutions, must first be verified with zero strain tests. The software will need to be able to accurately and precisely measure the three-dimensional strain in a specimen with zero strain and in a specimen with zero strain but rigid body motion.

Once validated, the software can be applied to the 2 N and 7 N image stacks to measure the local strain (Fig. 7.1). Each specimen experienced macroscopic deformations, but it is not yet known what occurred internally and how the strains may vary depending on the geometry of the bone.

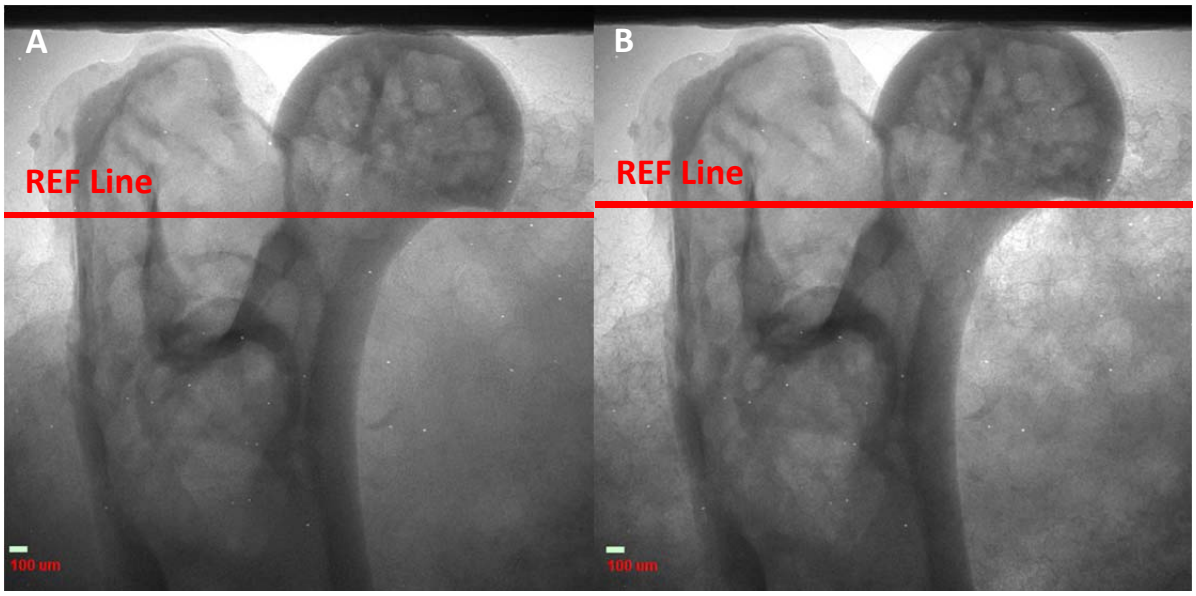

Figure 7.1: MicroCT projection images of the 2 N and 7 N step mechanical test. (A) The 2 N image stack will serve as the reference for the DVC analysis. (B) The 7 N or deformed image stack will be compared to the reference image stack in the DVC analysis.

REFERENCES

Ammann, P. & Rizzoli, R., 2003. Bone strength and its determinants. *Osteoporosis international*, 14 Suppl 3, pp.S13–S18.

Bagi, C.M. et al., 2006. The use of micro-CT to evaluate cortical bone geometry and strength in nude rats: Correlation with mechanical testing, pQCT and DXA. *Bone*, 38(1), pp.136–144.

Basler, S.E. et al., 2011. Towards validation of computational analyses of peri-implant displacements by means of experimentally obtained displacement maps. *Computer methods in biomechanics and biomedical engineering*, 14(March 2015), pp.165–174.

Bay, B.K. et al., 1999. Digital volume correlation: Three-dimensional strain mapping using X-ray tomography. *Experimental Mechanics*, 39(3), pp.217–226.

Beck, T.J. et al., 2000. Structural trends in the aging femoral neck and proximal shaft: analysis of the Third National Health and Nutrition Examination Survey dual-energy X-ray absorptiometry data. *Journal of bone and mineral research : the official journal of the American Society for Bone and Mineral Research*, 15(12), pp.2297–2304.

Bergmann, G. et al., 2001. Hip forces and gait patterns from rountine activities. *Journal of Biomechanics*, 34, pp.859–871.

Bergmann, G., Graichen, F. & Rohlmann, A., 1993. Hip joint loading during walking and running, measured in two patients. *Journal of Biomechanics*, 26(8), pp.969–990.

Bessho, M. et al., 2007. Prediction of strength and strain of the proximal femur by a CT-based finite element method. *Journal of Biomechanics*, 40(8), pp.1745–1753.

Bousson, V. et al., 2004. Cortical bone in the human femoral neck: three-dimensional appearance and porosity using synchrotron radiation. *Journal of bone and mineral research : the official journal of the American Society for Bone and Mineral Research*, 19(5), pp.794–801.

Bouxsein, M.L., 2003. Bone quality: where do we go from here? *Osteoporosis International*, 14(0), pp.118–127. Available at: http://link.springer.com/10.1007/s00198-003-1489-x.

Burge, R. et al., 2007. Incidence and Economic Burden of Osteoporosis-Related Fractures in the United States, 2005–2025. *Journal of Bone and Mineral Research*, 22(3), pp.465–475. Available at: http://onlinelibrary.wiley.com/doi/10.1359/jbmr.061113/epdf.

Burr, D.B. et al., 1996. In vivo measurement of human tibial strains during vigorous activity.

Bone, 18(5), pp.405–410.

Carriero, A. et al., 2014. Ex vivo determination of bone tissue strains for an in vivo mouse tibial loading model. *Journal of Biomechanics*, 47(10), pp.2490–2497. Available at: http://dx.doi.org/10.1016/j.jbiomech.2014.03.035.

Christen, D. et al., 2012. Deformable image registration and 3D strain mapping for the quantitative assessment of cortical bone microdamage. *Journal of the Mechanical Behavior of Biomedical Materials*, 8, pp.184–193. Available at: http://dx.doi.org/10.1016/j.jmbbm.2011.12.009.

Ciarelli, M.J. et al., 1991. Evaluation of orthogonal mechanical properties and density of human trabecular bone from the major metaphyseal regions with materials testing and computed tomography. *Journal of orthopaedic research : official publication of the Orthopaedic Research Society*, 9(5), pp.674–682.

Cody, D.D. et al., 1999. Femoral strength is better predicted by finite element models than QCT and DXA. *Journal of Biomechanics*, 32(10), pp.1013–1020.

Cole, J.H. & Van Der Meulen, M.C.H., 2011. Whole bone mechanics and bone quality. *Clinical Orthopaedics and Related Research*, 469(8), pp.2139–2149.

Cooper, C. et al., 2011. Secular trends in the incidence of hip and other osteoporotic fractures. *Osteoporosis International*, 22(5), pp.1277–1288.

Cordey, J. & Gautier, E., 1999a. Strain gauges used in the mechanical testing of bones Part I: Theoretical and technical aspects. *Injury*, 30(99), pp.SA7–SA13. Available at: http://www.sciencedirect.com/science/article/pii/S0020138399001205.

Cordey, J. & Gautier, E., 1999b. Strain gauges used in the mechanical testing of bones Part II: "In vitro" and "in vivo" technique. *Injury*, 30, pp.SA14–SA20. Available at: http://www.sciencedirect.com/science/article/pii/S0020138399001217.

Courtney, a C. et al., 1995. Age-related reductions in the strength of the femur tested in a fall-loading configuration. *The Journal of bone and joint surgery. American volume*, 77(3), pp.387–395.

Cristofolini, L. et al., 2008. Multiscale investigation of the functional properties of the human femur. *Philosophical transactions. Series A, Mathematical, physical, and engineering sciences*, 366(1879), pp.3319–41. Available at: http://www.ncbi.nlm.nih.gov/pubmed/18593659.

Cristofolini, L. et al., 2009. Strain distribution in the proximal human femoral metaphysis. *Proceedings of the Institution of Mechanical Engineers, Part H: Journal of Engineering in Medicine*, 223(3), pp.273–288. Available at: http://pih.sagepub.com/lookup/doi/10.1243/09544119JEIM497 [Accessed September 22, 2014].

Cummings, S.R. & Iii, L.J.M., 2002. Epidemiology and outcomes of osteoporotic fractures. , 359, pp.1761–1767.

Dall'Ara, E., Barber, D. & Viceconti, M., 2014. About the inevitable compromise between spatial resolution and accuracy of strain measurement for bone tissue: A 3D zero-strain study. *Journal of Biomechanics*, 47(12), pp.2956–2963. Available at: http://dx.doi.org/10.1016/j.jbiomech.2014.07.019.

Dickinson, A.S., Taylor, A.C. & Browne, M., 2012. The influence of acetabular cup material on pelvis cortex surface strains, measured using digital image correlation. *Journal of Biomechanics*, 45(4), pp.719–723. Available at: http://dx.doi.org/10.1016/j.jbiomech.2011.11.042.

Ding, M. et al., 1997. Age variations in the properties of human tibial trabecular bone. *The Journal of bone and joint surgery. British volume*, 79(6), pp.995–1002.

Esses, S.I., Lotz, J.C. & Hayes, W.C., 1989. Biomechanical properties of the proximal femur determined in vitro by single-energy quantitative computed tomography. *J Bone Miner Res*, 4(5), pp.715–722.

Felsenberg, D. & Boonen, S., 2005. The bone quality framework: Determinants of bone strength and their interrelationships, and implications for osteoporosis management. *Clinical Therapeutics*, 27(1), pp.1–11.

Field, R.E. & Rushton, N., 1989. Proximal femoral surface strain gauge analysis of a new epiphyseal prosthesis. *Journal of Biomedical Engineering*, 11(2), pp.123–129.

Filardi, S. et al., 2004. Femoral neck fragility in women has its structural and biomechanical basis established by periosteal modeling during growth and endocortical remodeling during aging. *Osteoporosis International*, 15(2), pp.103–107.

Florschutz, A. V et al., 2015. Femoral Neck Fractures : Current Management. *J Orthop Trauma*, 29(3), pp.121–129.

Földhazy, Z. et al., 2005. Exercise-induced strain and strain rate in the distal radius. *J Bone Joint*

Surg Br, 87-b(2), pp.261–266.

Galante, J., Rostoker, W. & Ray, R.D., 1970. Physical properties of trabecular bone. *Calcified Tissue Research*, 5(1), pp.236–246.

Gilchrist, S., Guy, P. & Cripton, P. a, 2013. Development of an inertia-driven model of sideways fall for detailed study of femur fracture mechanics. *Journal of biomechanical engineering*, 135(12), p.121001. Available at: http://www.ncbi.nlm.nih.gov/pubmed/24026221.

Gillard, F. et al., 2014. The application of digital volume correlation (DVC) to study the microstructural behaviour of trabecular bone during compression. *Journal of the Mechanical Behavior of Biomedical Materials*, 29, pp.480–499. Available at: http://dx.doi.org/10.1016/j.jmbbm.2013.09.014.

Grassi, L. & Isaksson, H., 2015. Extracting accurate strain measurements in bone mechanics: A critical review of current methods. *Journal of the Mechanical Behavior of Biomedical Materials*, 50, pp.43–54. Available at: http://dx.doi.org/10.1016/j.jmbbm.2015.06.006.

Hahn, M. et al., 1992. Trabecular bone pattern factor-a new parameter for simple quantification of bone microarchitecture. *Bone*, 13(4), pp.327–330.

Hardisty, M.R., 2009. Whole Bone Strain Quantification by Image Registration: A Validation Study. *Journal of Biomechanical Engineering*, 131(6), p.064502. Available at: http://biomechanical.asmedigitalcollection.asme.org/article.aspx?doi=10.1115/1.3127249.

Helgason, B. et al., 2008. Mathematical relationships between bone density and mechanical properties: A literature review. *Clinical Biomechanics*, 23(2), pp.135–146.

Hildebrand, T. et al., 1999. Direct Three-Dimensional Morphometric Analysis of Human Cancellous Bone: Microstructural Data from Spine, Femur, Iliac Crest, and Calcaneus. *Journal of Bone and Mineral Research*, 14(7), pp.1167–1174. Available at: http://doi.wiley.com/10.1359/jbmr.1999.14.7.1167.

Huiskes, R. & Chao, E.Y.S., 1983. a Survey of Finite Element Analysis in Orthopedic Biomechanics: the First Decade. *J Biomechanics*, 16(6), pp.385–409.

Hussein, A.I., Barbone, P.E. & Morgan, E.F., 2012. Digital volume correlation for study of the mechanics of whole bones. *Procedia IUTAM*, 4, pp.116–125. Available at: http://dx.doi.org/10.1016/j.piutam.2012.05.013.

Imai, K., 2015. Computed tomography-based finite element analysis to assess fracture risk and osteoporosis treatment. *World journal of experimental medicine*, 5(3), pp.182–7. Available

at:
http://www.pubmedcentral.nih.gov/articlerender.fcgi?artid=4543812&tool=pmcentrez&rendertype=abstract.

Ito, M., 2011. Recent progress in bone imaging for osteoporosis research. *Journal of Bone and Mineral Metabolism*, 29(2), pp.131–140.

Jämsä, T. et al., 1999. Femoral neck is a sensitive indicator of bone loss in immobilized hind limb of mouse. *Journal of bone and mineral research : the official journal of the American Society for Bone and Mineral Research*, 14(10), pp.1708–13. Available at: http://www.ncbi.nlm.nih.gov/pubmed/10491218.

Jämsä, T., Tuukkanen, J. & Jalovaara, P., 1998. Femoral neck strength of mouse in two loading configurations: Method evaluation and fracture characteristics. *Journal of Biomechanics*, 31(8), pp.723–729.

Jandejsek, I., Jirou??ek, O. & Vav????k, D., 2011. Precise strain measurement in complex materials using digital volumetric correlation and time lapse micro-CT data. *Procedia Engineering*, 10, pp.1730–1735.

John, D.C., 2003. Role of collagen and other organics in the mechanical properties of bone. *Osteoporosis international : a journal established as result of cooperation between the European Foundation for Osteoporosis and the National Osteoporosis Foundation of the USA*, 14 Suppl 5, pp.S29–S36. Available at: http://www.ncbi.nlm.nih.gov/pubmed/14504703.

Keaveny, T.M. et al., 1997. Systematic and random errors in compression testing of trabecular bone. *Journal of Orthopaedic Research*, 15(1), pp.101–110.

Kersh, M.E. et al., 2013. The heterogeneity in femoral neck structure and strength. *Journal of Bone and Mineral Research*, 28(5), pp.1022–1028.

Keyak, J.H., 2001. Improved prediction of proximal femoral fracture load using nonlinear finite element models. *Medical Engineering & Physics*, 23(3), pp.165–73. Available at: http://www.ncbi.nlm.nih.gov/pubmed/11410381.

Keyak, J.H. et al., 1998. Prediction of femoral fracture load using automated finite element modeling. *J Biomechanics*, 31, pp.125 – 133.

Keyak, J.H. et al., 1993. Validation of an automated method of three-dimensional finite element modelling of bone. *Journal of Biomedical Engineering*, 15(6), pp.505–509.

Kopperdahl, D.L. & Keaveny, T.M., 1998. Yield strain behavior of trabecular bone. *Journal of Biomechanics*, 31(7), pp.601–608.

Lang, T.F. et al., 1997. Volumetric quantitative computed tomography of the proximal femur: Precision and relation to bone strength. *Bone*, 21(1), pp.101–108.

Lanyon, L.E. et al., 1975. Bone deformation recorded in vivo from strain gauges attached to the human tibial shaft. *Acta orthopaedica Scandinavica*, 46(2), pp.256–68. Available at: http://www.ncbi.nlm.nih.gov/pubmed/1146518.

Linde, F., Hvid, I. & Madsen, F., 1992. The effect of specimen geometry on the mechanical behaviour of trabecular bone specimens. *Journal of Biomechanics*, 25(4), pp.359–368.

Liu, L. & Morgan, E.F., 2007. Accuracy and precision of digital volume correlation in quantifying displacements and strains in trabecular bone. *Journal of Biomechanics*, 40(15), pp.3516–3520.

Liu, X.S. et al., 2010. Individual Trabeculae Segmentation (ITS)-based morphological analysis of high-resolution peripheral quantitative computed tomography images detects abnormal trabecular plate and rod microarchitecture in premenopausal women with idiopathic osteoporosis. *Journal of Bone and Mineral Research*, 25(7), pp.1496–1505.

Lochmüller, E.M. et al., 2000. In situ femoral dual-energy X-ray absorptiometry related to ash weight, bone size and density, and its relationship with mechanical failure loads of the proximal femur. *Osteoporosis International*, 11(4), pp.361–367.

Lotz, J.C., Cheal, E.J. & Hayes, W.C., 1995. Stress distributions within the proximal femur during gait and falls: Implications for osteoporotic fracture. *Osteoporosis International*, 5(4), pp.252–261.

Lotz, J.C. & Hayes, W.C., 1990. The use of quantitative computed tomography to estimate risk of fracture of the hip from falls Use of Quantitative to Estimate Computed Risk Tomography of Fracture of the Hip from. *The Journal of Bone & Joint Surgery*, 72(5), pp.689–700.

Madi, K. et al., 2013. Computation of full-field displacements in a scaffold implant using digital volume correlation and finite element analysis. *Medical Engineering and Physics*, 35(9), pp.1298–1312.

Martelli, S. et al., 2014. Strain energy in the femoral neck during exercise. *Journal of Biomechanics*, 47(8), pp.1784–1791. Available at:

http://dx.doi.org/10.1016/j.jbiomech.2014.03.036.

Mccreadie, B.R. & Goldstein, S.A., 2000. Biomechanics of Fracture: Is Bone Mineral Density Sufficient to Assess Risk? *Journal of Bone and Mineral Research*, 15(12), pp.2305–2308. Available at: http://doi.wiley.com/10.1359/jbmr.2000.15.12.2305.

Mittra, E., Rubin, C. & Qin, Y.X., 2005. Interrelationship of trabecular mechanical and microstructural properties in sheep trabecular bone. *Journal of Biomechanics*, 38(6), pp.1229–1237.

Morgan, E.F., Bayraktar, H.H. & Keaveny, T.M., 2003. Trabecular bone modulus-density relationships depend on anatomic site. *Journal of Biomechanics*, 36(7), pp.897–904.

Müller, R., 2009. Hierarchical microimaging of bone structure and function. *Nature reviews. Rheumatology*, 5(7), pp.373–381. Available at: http://dx.doi.org/10.1038/nrrheum.2009.107.

Van Den Munckhof, S. & Zadpoor, A.A., 2014. How accurately can we predict the fracture load of the proximal femur using finite element models? *Clinical Biomechanics*, 29(4), pp.373–380. Available at: http://dx.doi.org/10.1016/j.clinbiomech.2013.12.018.

Natali, A.N. & Meroi, E.A., 1989. A review of the biomechanical properties of bone as a material. *Journal of Biomedical Engineering*, 11(4), pp.266–276.

Nelson, D. a et al., 2004. Comparison of cross-sectional geometry of the proximal femur in white and black women from Detroit and Johannesburg. *Journal of bone and mineral research : the official journal of the American Society for Bone and Mineral Research*, 19(4), pp.560–5. Available at: http://www.ncbi.nlm.nih.gov/pubmed/15005842.

Nielsen, S.P., 2000. Review Article The Fallacy of BMD : A Critical Review of the Diagnostic Use of Dual. *Clinical Physiology*, pp.174–183.

Odgaard, A. & Gundersen, H.J.G., 1993. Quantification of connectivity in cancellous bone, with special emphasis on 3-D reconstructions. *Bone*, 14(2), pp.173–182.

Op Den Buijs, J. & Dragomir-Daescu, D., 2011. Validated finite element models of the proximal femur using two-dimensional projected geometry and bone density. *Computer Methods and Programs in Biomedicine*, 104(2), pp.168–174.

Parfitt, A.M., 1992. Implications of architecture for the pathogenesis and prevention of vertebral fracture. *Bone*, 13(SUPPL. 2), pp.41–47.

Peng, L. et al., 2006. Comparison of isotropic and orthotropic material property assignments on

femoral finite element models under two loading conditions. *Medical Engineering and Physics*, 28(3), pp.227–233.

Perilli, E. et al., 2007. MicroCT examination of human bone specimens: Effects of polymethylmethacrylate embedding on structural parameters. *Journal of Microscopy*, 225(2), pp.192–200.

Perry, C.C., 1986. Strain-Gage Reinforcement Effects on Orthotropic Materials. *Experimental Techniques*, (February), pp.20 – 24.

Pistoia, W., Van Rietbergen, B. & Rüegsegger, P., 2003. Mechanical consequences of different scenarios for simulated bone atrophy and recovery in the distal radius. *Bone*, 33(6), pp.937–945.

Prendergast, P.J., 1997. Finite element models in tissue mechanics and orthopaedic implant design. *Clinical Biomechanics*, 12(6), pp.343–366.

Rho, J.Y., Kuhn-Spearing, L. & Zioupos, P., 1998. Mechanical properties and the hierarchical structure of bone. *Medical Engineering and Physics*, 20(2), pp.92–102.

Schileo, E. et al., 2007. Subject-specific finite element models can accurately predict strain levels in long bones. *Journal of Biomechanics*, 40(13), pp.2982–2989.

Seeman, E. & Delmas, P.D., 2006. Bone quality--the material and structural basis of bone strength and fragility. *The New England journal of medicine*, 354(21), pp.2250–2261.

SEER, 2011. Compact bone & spongy bone. *U.S. National Cancer Institute's Surveillance, Epidemiology and End Results (SEER) Program*. Available at: https://commons.wikimedia.org/wiki/File:Illu_compact_spongy_bone.jpg.

Sernbo, I. & Johnell, O., 1993a. Consequences of a Hip Fracture: A Prospective Study over 1 Year. *Osteoporosis International*, 3, pp.148–153.

Sernbo, I. & Johnell, O., 1993b. International Original Article Consequences of a Hip Fracture : A Prospective Study over 1 Year. *Osteoporosis International*, pp.148–153.

De Souza, R.L. et al., 2005. Non-invasive axial loading of mouse tibiae increases cortical bone formation and modifies trabecular organization: A new model to study cortical and cancellous compartments in a single loaded element. *Bone*, 37(6), pp.810–818.

Sztefek, P. et al., 2010. Using digital image correlation to determine bone surface strains during loading and after adaptation of the mouse tibia. *Journal of Biomechanics*, 43(4), pp.599–605. Available at: http://dx.doi.org/10.1016/j.jbiomech.2009.10.042.

Tang, T. et al., 2015. Shear deformation and fracture of human cortical bone. *Bone*, 71, pp.25–35. Available at: http://dx.doi.org/10.1016/j.bone.2014.10.001.

Theobald, T.M. et al., 1998. International Original Article Black – White Differences in Hip Geometry. *Osteoporosis International*, pp.61–67.

Thompson, M.S. et al., 2007. Digital image correlation: A technique for determining local mechanical conditions within early bone callus. *Medical Engineering and Physics*, 29(7), pp.820–823.

Turner, C.H. et al., 2000. Genetic regulation of cortical and trabecular bone strength and microstructure in inbred strains of mice. *Journal of bone and mineral research : the official journal of the American Society for Bone and Mineral Research*, 15(6), pp.1126–1131.

Voide, R., Van Lenthe, G.H. & Müller, R., 2008. Differential effects of bone structural and material properties on bone competence in C57BL/6 and C3H/He inbred strains of mice. *Calcified Tissue International*, 83(1), pp.61–69.

Wainwright, S.A. et al., 2005. Hip Fracture in Women without Osteoporosis. *J Clin Endocrinol Metab*, 90(5), pp.2787–2793. Available at: http://jcem.endojournals.org/cgi/content/abstract/90/5/2787.

Wang, X. & Ni, Q., 2003. Determination of cortical bone porosity and pore size distribution using a low field pulsed NMR approach. *Journal of Orthopaedic Research*, 21(2), pp.312–319.

Wang, X.F. et al., 2005. Varying contributions of growth and ageing to racial and sex differences in femoral neck structure and strength in old age. *Bone*, 36(6), pp.978–986.

Wentzell.S, Nesbitt. R.S, Macione.J, Knapp. R, K.S.., 2011. Bone Strain Measurement Using 3D Digital Image Correlation of Second Harmonic Generation Images. *2011 IEEE 37th Annual Northeast Bioengineering Conference (NEBEC)*, pp.3–4.

Wentzell, S. et al., 2015. Measurement of lacunar bone strains and crack formation during tensile loading by digital volume correlation of second harmonic generation images. *Journal of the Mechanical Behavior of Biomedical Materials*, c, pp.148–156. Available at: http://linkinghub.elsevier.com/retrieve/pii/S1751616115005019.

Yang, P.F., Brüggemann, G. & Rittweger, J., 2011. What do we currently know from in vivo bone strain measurements in humans? *J Musculoskelet Neuronal Interact*, 11(1), pp.8–20.

Yoshikawa, T. et al., 1994. Geometric structure of the femoral neck measured using dual-energy

x-ray absorptiometry. *Journal of Bone and Mineral Research*, 9(7), pp.1053–64. Available at: http://onlinelibrary.wiley.com/doi/10.1002/jbmr.5650090713/abstract\nhttp://www.ncbi.nlm.nih.gov/pubmed/7942152.

Zysset, P.K., 2003. A review of morphology-elasticity relationships in human trabecular bone: Theories and experiments. *Journal of Biomechanics*, 36(10), pp.1469–1485.

APPENDIX A: FORCE-DISPLACEMENT CURVE OF STEP MECHANICAL TEST

The step mechanical testing data was not used in this study, but will be analyzed in following studies to complete the main objective identified in Chapter 1. Figure A.1 – A.10 correspond to the force-displacement curves of specimens 1 through 10.

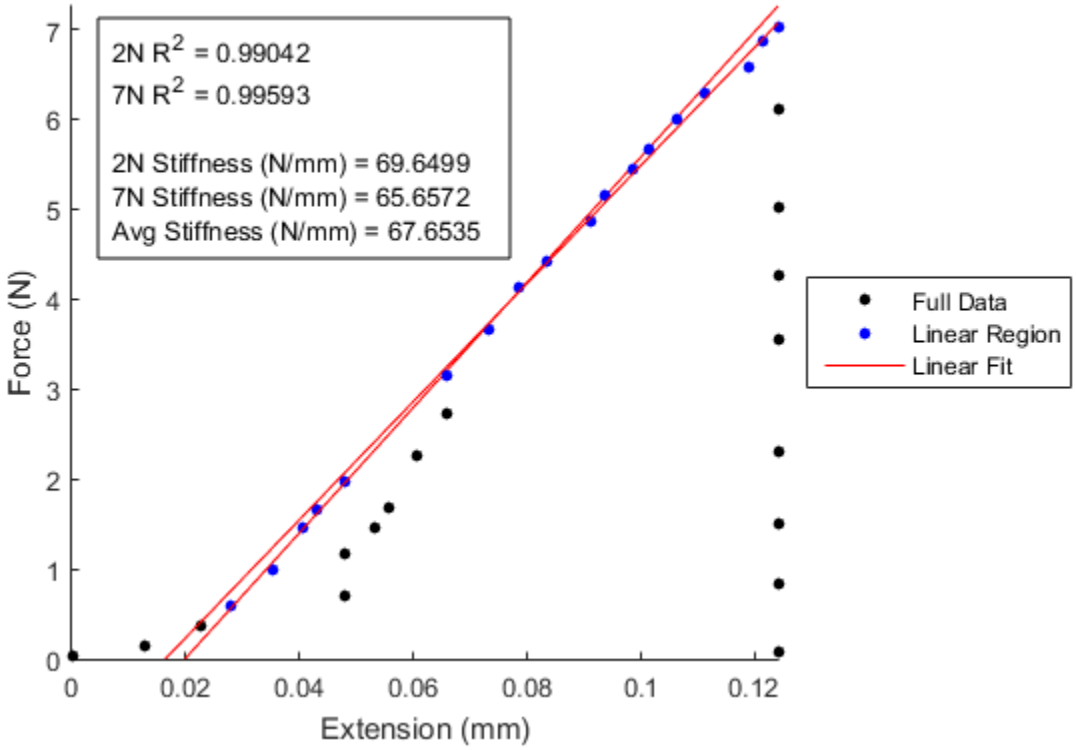

Figure A.1: The force-displacement(extension) curve of the step mechanical test with linear regressions overlaying the 2 N and 7 N loading timeframes. The stiffness of specimen 1 during the 2 N and 7 N loading phases were 69.65 N and 65.66 N, respectively.

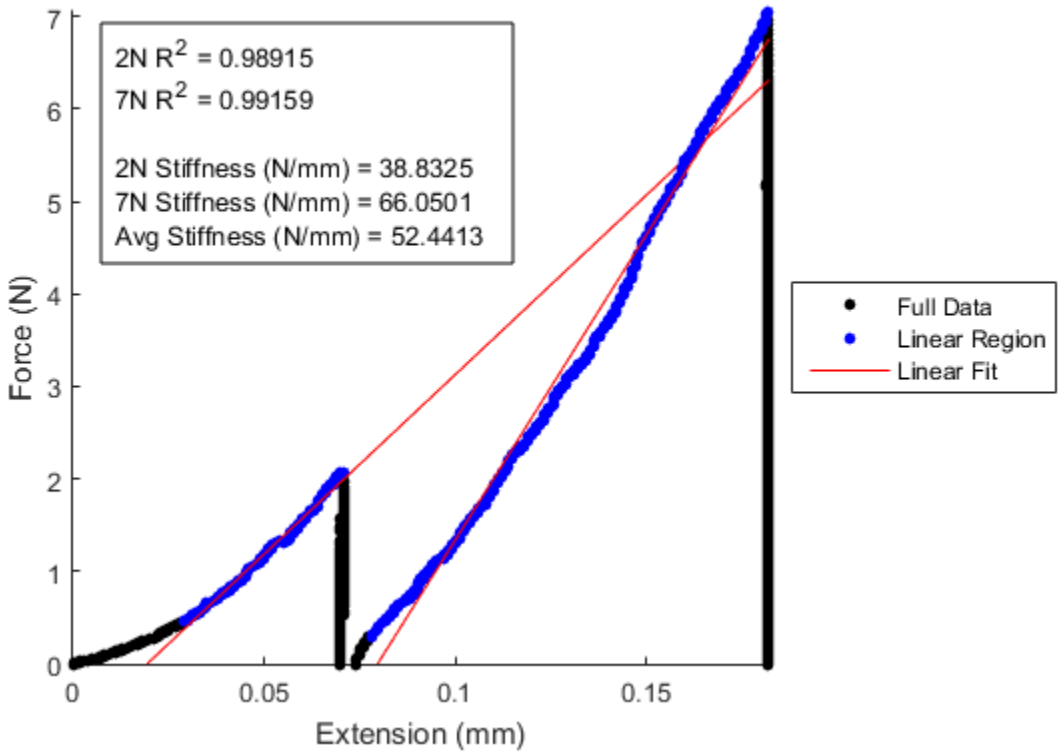

Figure A.2: The force-displacement(extension) curve of the step mechanical test with linear regressions overlaying the 2 N and 7 N loading timeframes. The stiffness of specimen 2 during the 2 N and 7 N loading phases were 38.83 N and 66.05 N, respectively.

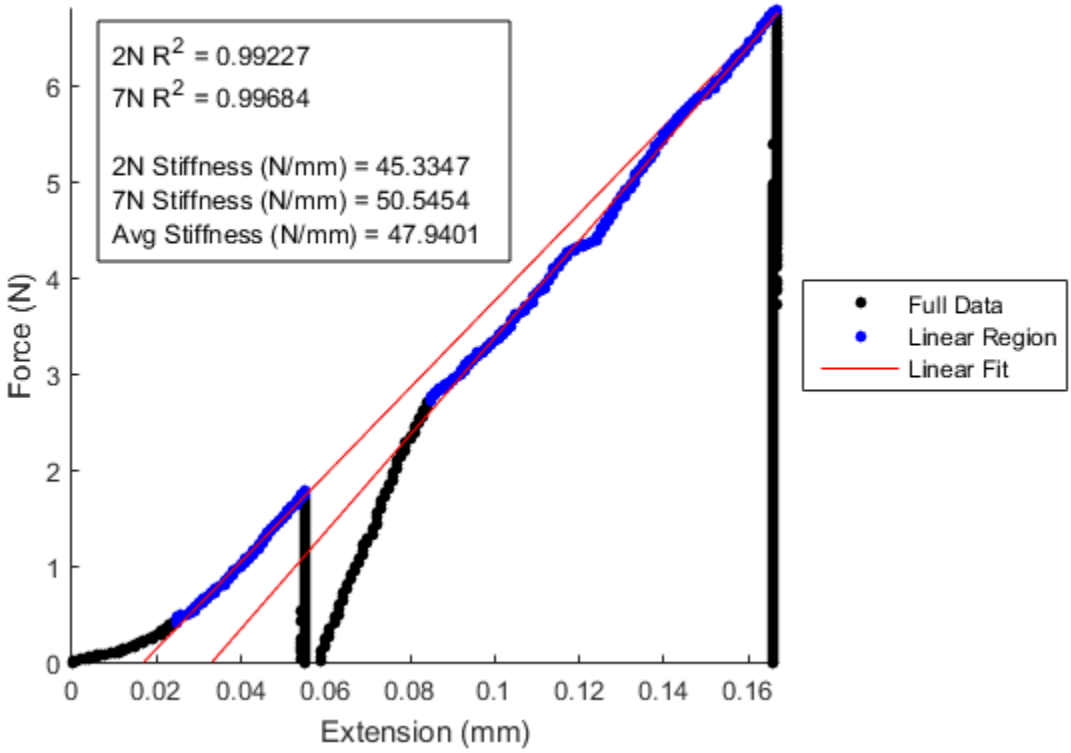

Figure A.3: The force-displacement(extension) curve of the step mechanical test with linear regressions overlaying the 2 N and 7 N loading timeframes. The stiffness of specimen 3 during the 2 N and 7 N loading phases were 45.33 N and 50.55 N, respectively.

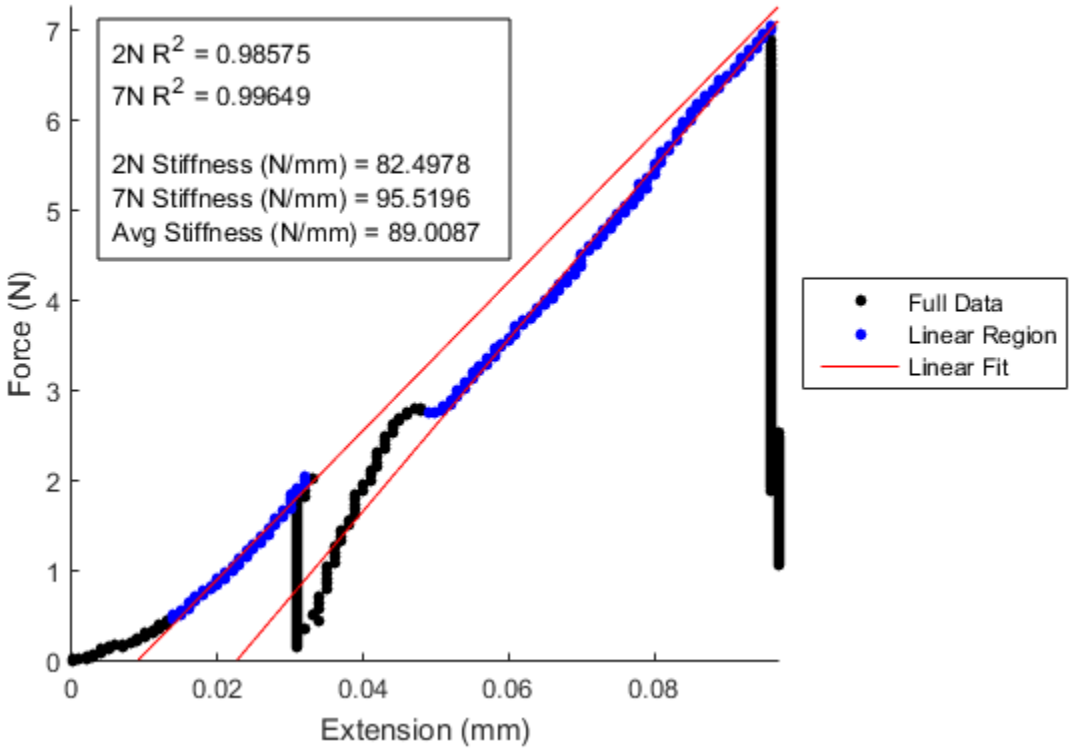

Figure A.4: The force-displacement(extension) curve of the step mechanical test with linear regressions overlaying the 2 N and 7 N loading timeframes. The stiffness of specimen 4 during the 2 N and 7 N loading phases were 82.50 N and 95.52 N, respectively.

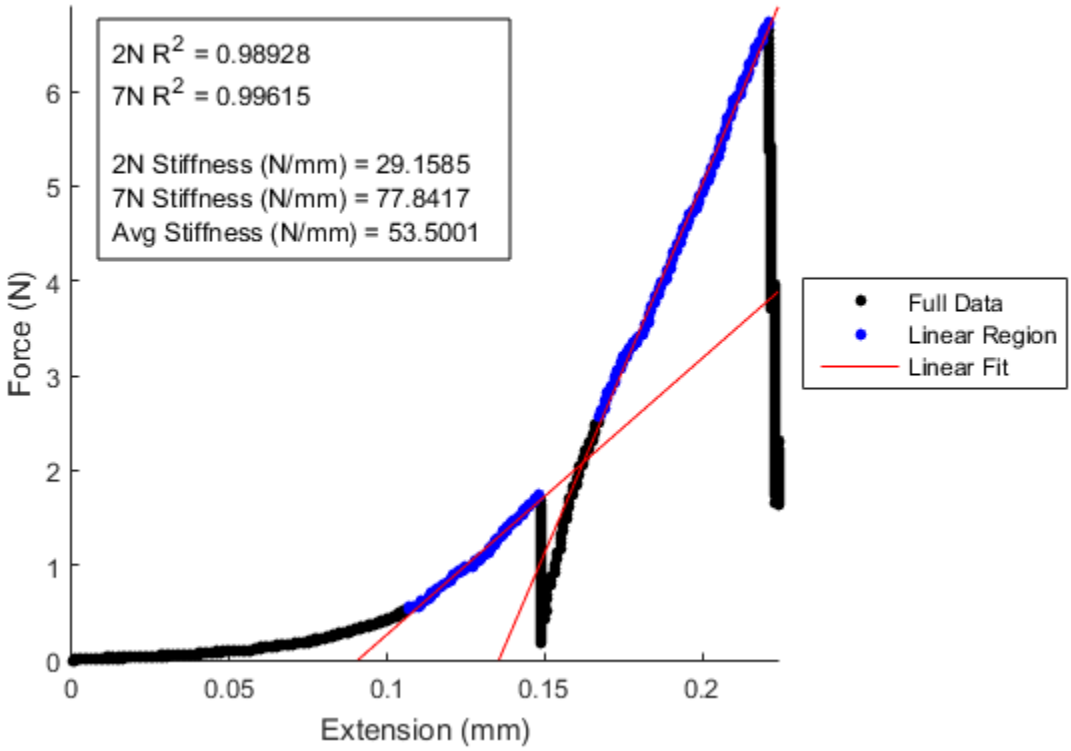

Figure A.5: The force-displacement(extension) curve of the step mechanical test with linear regressions overlaying the 2 N and 7 N loading timeframes. The stiffness of specimen 5 during the 2 N and 7 N loading phases were 29.16 N and 77.84 N, respectively.

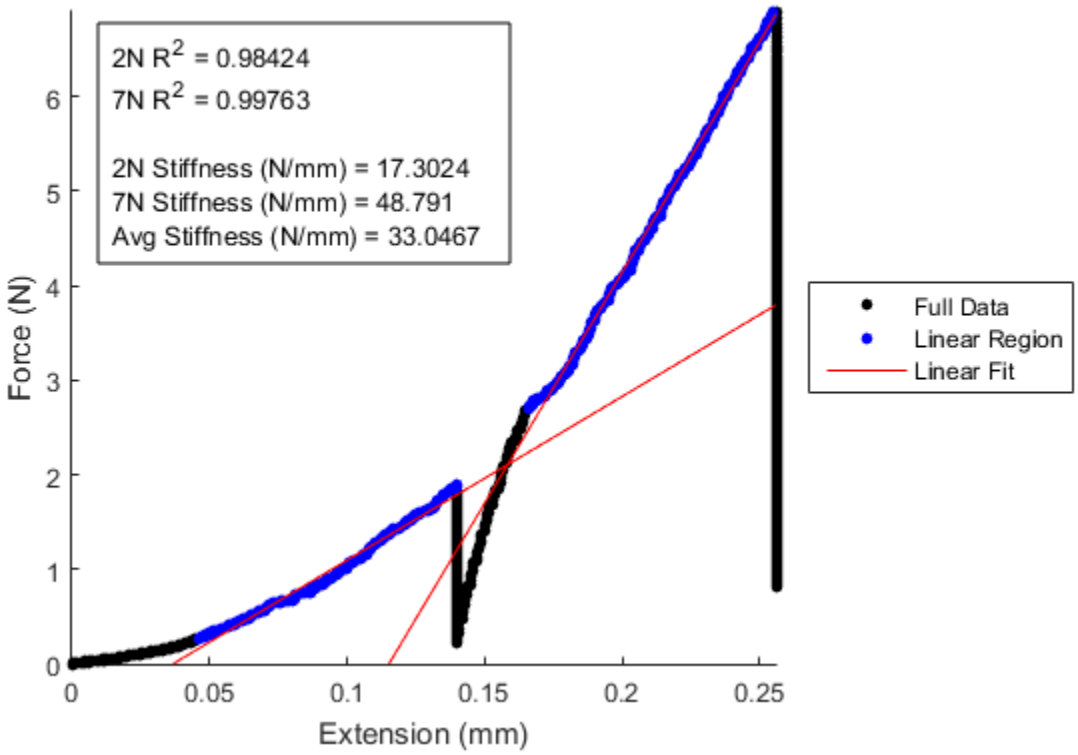

Figure A.6: The force-displacement(extension) curve of the step mechanical test with linear regressions overlaying the 2 N and 7 N loading timeframes. The stiffness of specimen 6 during the 2 N and 7 N loading phases were 17.30 N and 48.79 N, respectively.

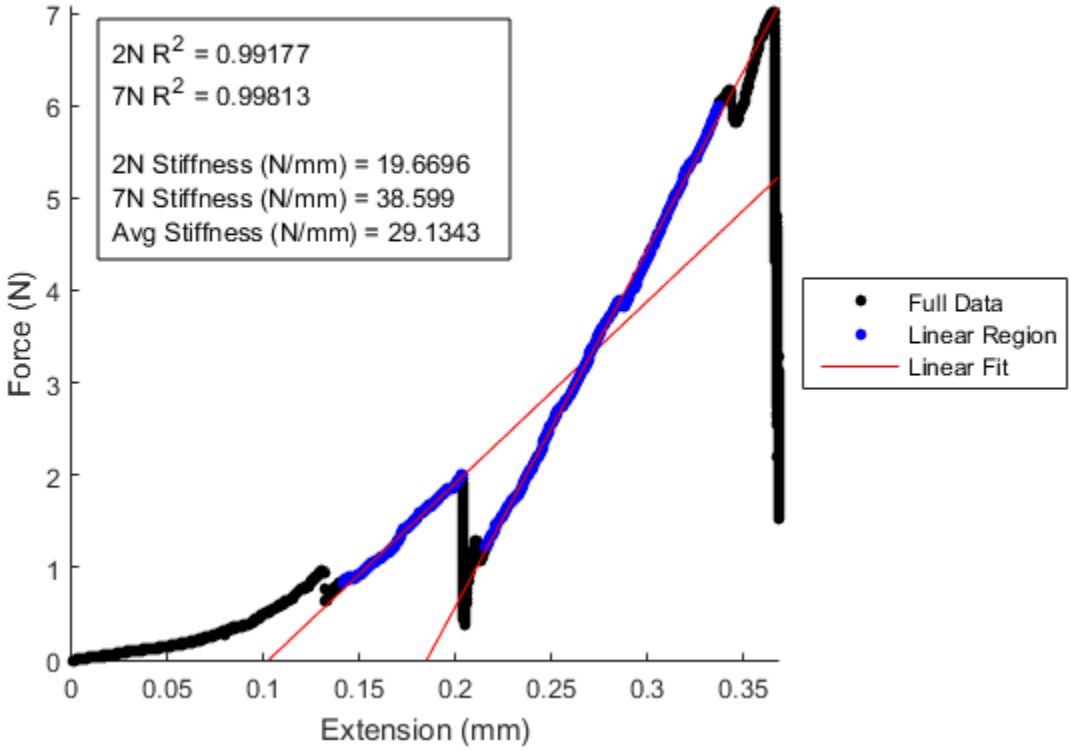

Figure A.7: The force-displacement(extension) curve of the step mechanical test with linear regressions overlaying the 2 N and 7 N loading timeframes. The stiffness of specimen 7during the 2 N and 7 N loading phases were 19.67 N and 38.60 N, respectively.

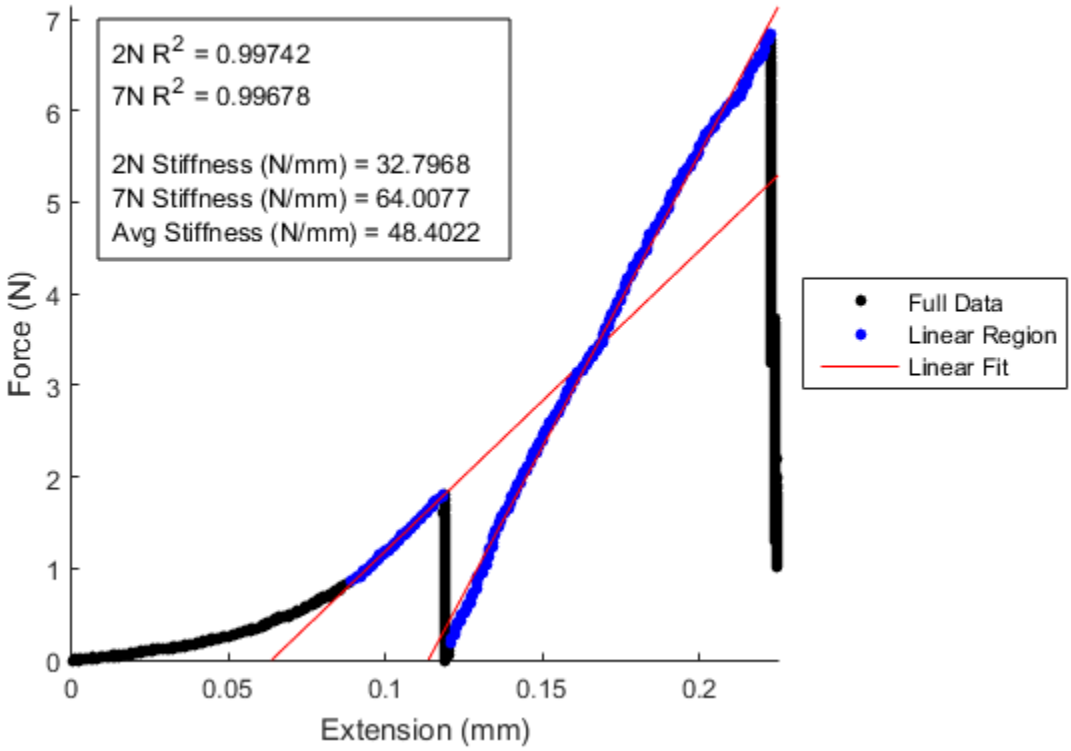

Figure A.8: The force-displacement(extension) curve of the step mechanical test with linear regressions overlaying the 2 N and 7 N loading timeframes. The stiffness of specimen 8 during the 2 N and 7 N loading phases were 32.80 N and 64.01 N, respectively.

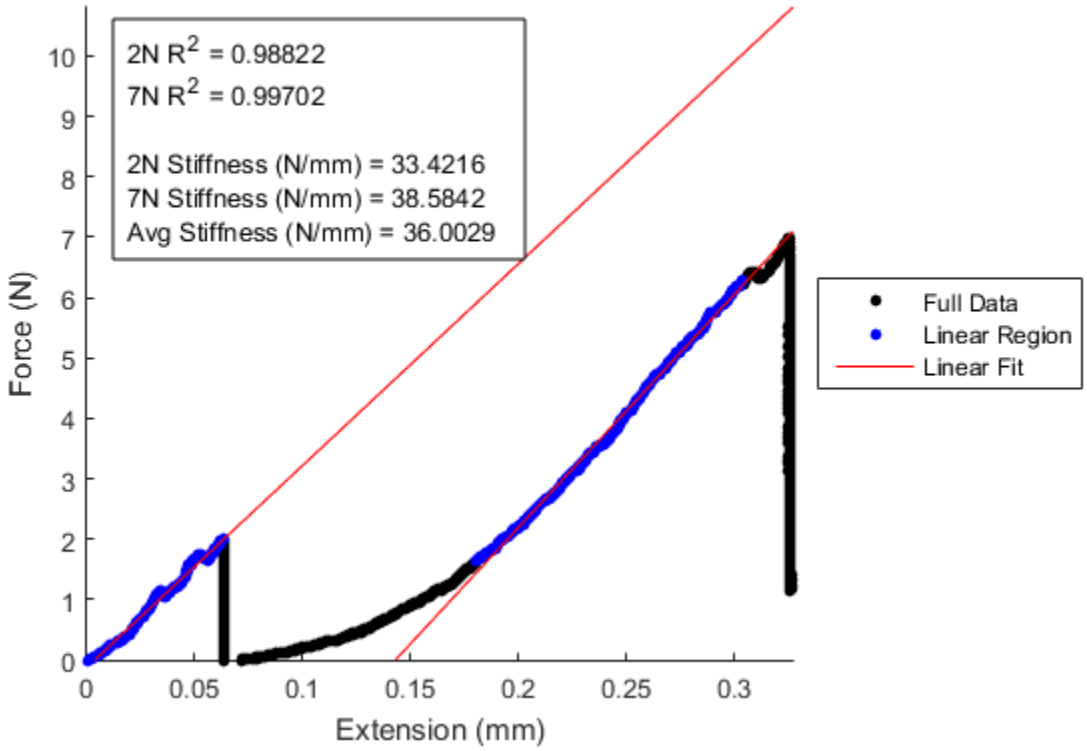

Figure A.9: The force-displacement(extension) curve of the step mechanical test with linear regressions overlaying the 2 N and 7 N loading timeframes. The stiffness of specimen 9 during the 2 N and 7 N loading phases were 33.42 N and 38.58 N, respectively.

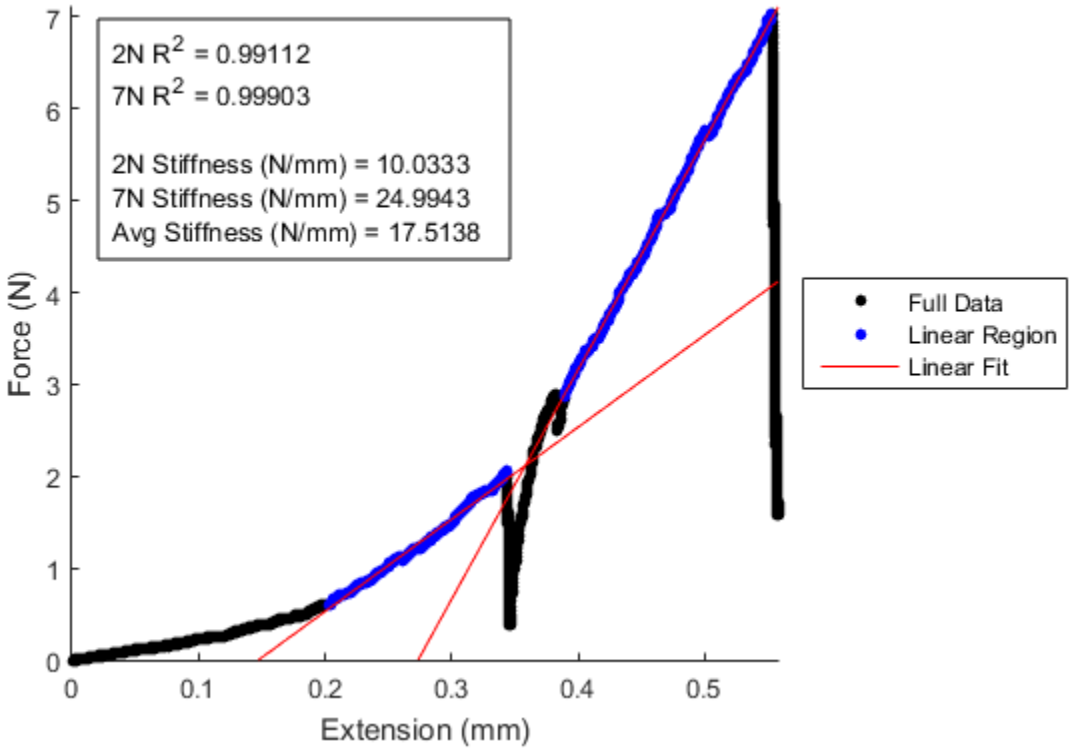

Figure A.10: The force-displacement(extension) curve of the step mechanical test with linear regressions overlaying the 2 N and 7 N loading timeframes. The stiffness of specimen 10 during the 2 N and 7 N loading phases were 10.03 N and 24.99 N, respectively.

APPENDIX B: RAW DATA OF STRUCTUAL PARAMETERS ALONG FEMORAL NECK

The raw data of the structural analysis is presented below in Table B.1 – B.6. Each variable was measured in 10% increments starting at the femoral neck closest to the trochanter (0% position) and ending at the femoral neck closest to the femoral head (100%).

Table B.1: Raw Specimen Data of Major Diameter (mm) along Femoral Neck

Specimen	Position along femoral neck										
	0%	10%	20%	30%	40%	50%	60%	70%	80%	90%	100%
1	1.229	1.106	1.015	0.967	0.942	0.934	0.943	0.968	1.013	1.112	1.213
2	1.253	1.082	1.003	0.941	0.898	0.874	0.875	0.894	0.928	0.994	1.108
3	1.150	1.007	0.923	0.879	0.860	0.862	0.911	0.993	1.065	1.162	1.204
4	1.057	0.986	0.950	0.930	0.926	0.929	0.943	0.971	1.007	1.060	1.135
5	1.167	1.123	1.094	1.077	1.071	1.065	1.072	1.082	1.098	1.124	1.161
6	1.056	1.017	0.995	0.979	0.971	0.970	0.971	0.976	0.994	1.015	1.046
7	1.249	1.138	1.069	1.009	0.961	0.957	0.967	0.992	1.049	1.120	1.213
8	1.233	1.171	1.127	1.089	1.059	1.036	1.022	1.016	1.042	1.070	1.110
9	1.078	1.010	0.973	0.949	0.931	0.926	0.937	0.955	0.982	1.033	1.107
10	1.164	1.082	1.021	0.982	0.958	0.934	0.926	0.937	0.981	1.033	1.104

Table B.2: Raw Specimen Data of Minor Diameter (mm) along Femoral Neck

Specimen	Position along femoral neck										
	0%	10%	20%	30%	40%	50%	60%	70%	80%	90%	100%
1	0.649	0.658	0.666	0.676	0.685	0.698	0.708	0.717	0.724	0.731	0.749
2	0.701	0.700	0.698	0.688	0.677	0.674	0.672	0.670	0.681	0.703	0.732
3	0.610	0.605	0.600	0.597	0.594	0.603	0.606	0.616	0.638	0.704	0.798
4	0.677	0.672	0.667	0.664	0.663	0.668	0.674	0.676	0.691	0.705	0.726
5	0.747	0.751	0.753	0.761	0.774	0.802	0.825	0.856	0.890	0.936	0.988
6	0.667	0.668	0.665	0.654	0.654	0.659	0.671	0.698	0.725	0.762	0.801
7	0.692	0.686	0.687	0.685	0.682	0.681	0.686	0.705	0.740	0.790	0.861
8	0.725	0.735	0.739	0.743	0.748	0.753	0.762	0.777	0.795	0.808	0.829
9	0.708	0.705	0.701	0.689	0.687	0.690	0.694	0.708	0.741	0.789	0.853
10	0.706	0.709	0.702	0.697	0.696	0.700	0.704	0.712	0.720	0.746	0.785

Table B.3: Raw Specimen Data of Cortical Thickness (mm) along Femoral Neck

Specimen	Position along femoral neck										
	0%	10%	20%	30%	40%	50%	60%	70%	80%	90%	100%
1	0.269	0.247	0.229	0.224	0.219	0.223	0.219	0.199	0.193	0.202	0.207
2	0.281	0.263	0.253	0.236	0.228	0.227	0.207	0.199	0.188	0.194	0.201
3	0.351	0.324	0.316	0.295	0.288	0.275	0.277	0.228	0.230	0.251	0.208
4	0.307	0.296	0.290	0.284	0.292	0.290	0.293	0.257	0.239	0.223	0.213
5	0.202	0.208	0.203	0.201	0.178	0.159	0.155	0.168	0.178	0.170	0.155
6	0.268	0.260	0.255	0.247	0.248	0.247	0.244	0.237	0.237	0.203	0.193
7	0.276	0.268	0.263	0.251	0.237	0.197	0.221	0.220	0.216	0.194	0.196
8	0.197	0.193	0.189	0.184	0.173	0.173	0.163	0.157	0.157	0.159	0.169
9	0.276	0.273	0.273	0.278	0.276	0.280	0.287	0.231	0.231	0.243	0.238
10	0.272	0.258	0.250	0.239	0.235	0.231	0.231	0.238	0.220	0.194	0.204

Table B.4: Raw Specimen Data of Cross Sectional Area (mm^2) along Femoral Neck

Specimen	Position along femoral neck										
	0%	10%	20%	30%	40%	50%	60%	70%	80%	90%	100%
1	0.605	0.560	0.526	0.510	0.505	0.510	0.521	0.540	0.568	0.625	0.696
2	0.668	0.587	0.545	0.505	0.474	0.461	0.459	0.468	0.493	0.543	0.627
3	0.543	0.475	0.433	0.411	0.400	0.406	0.426	0.467	0.516	0.614	0.728
4	0.549	0.515	0.494	0.483	0.480	0.486	0.498	0.514	0.544	0.584	0.643
5	0.668	0.652	0.639	0.637	0.644	0.662	0.687	0.719	0.759	0.819	0.894
6	0.541	0.525	0.512	0.496	0.493	0.497	0.508	0.532	0.563	0.605	0.655
7	0.662	0.607	0.572	0.539	0.509	0.510	0.520	0.549	0.606	0.688	0.813
8	0.691	0.668	0.648	0.632	0.619	0.609	0.608	0.616	0.643	0.670	0.714
9	0.590	0.555	0.533	0.511	0.499	0.500	0.509	0.530	0.569	0.637	0.736
10	0.637	0.599	0.560	0.536	0.522	0.512	0.511	0.520	0.547	0.596	0.667

Table B.5: Raw Specimen Data of Cortical Area (mm^2) along Femoral Neck

Specimen	Position along femoral neck										
	0%	10%	20%	30%	40%	50%	60%	70%	80%	90%	100%
1	0.481	0.440	0.414	0.402	0.398	0.402	0.412	0.417	0.405	0.432	0.475
2	0.546	0.488	0.455	0.418	0.394	0.391	0.395	0.389	0.385	0.425	0.492
3	0.516	0.454	0.418	0.393	0.381	0.378	0.389	0.401	0.419	0.499	0.560
4	0.499	0.469	0.452	0.441	0.443	0.445	0.456	0.466	0.484	0.505	0.525
5	0.491	0.481	0.488	0.493	0.493	0.502	0.510	0.519	0.551	0.593	0.645
6	0.464	0.449	0.438	0.421	0.420	0.424	0.434	0.458	0.484	0.505	0.528
7	0.535	0.502	0.479	0.450	0.417	0.400	0.425	0.437	0.466	0.507	0.585
8	0.453	0.436	0.431	0.424	0.431	0.423	0.418	0.416	0.424	0.440	0.476
9	0.503	0.481	0.469	0.455	0.445	0.449	0.460	0.462	0.486	0.540	0.586
10	0.524	0.492	0.461	0.439	0.426	0.418	0.420	0.448	0.482	0.506	0.553

Table B.6: Raw Specimen Data of Cortical Fraction (-) along Femoral Neck

Specimen	Position along femoral neck										
	0%	10%	20%	30%	40%	50%	60%	70%	80%	90%	100%
1	0.796	0.786	0.787	0.789	0.788	0.788	0.792	0.773	0.713	0.691	0.683
2	0.818	0.831	0.835	0.829	0.830	0.849	0.860	0.831	0.781	0.783	0.785
3	0.950	0.955	0.965	0.955	0.953	0.933	0.913	0.858	0.813	0.813	0.769
4	0.909	0.912	0.914	0.913	0.923	0.917	0.916	0.907	0.888	0.864	0.817
5	0.735	0.737	0.763	0.774	0.765	0.758	0.742	0.722	0.726	0.725	0.721
6	0.858	0.856	0.856	0.849	0.851	0.853	0.854	0.861	0.859	0.836	0.805
7	0.807	0.828	0.836	0.835	0.819	0.785	0.818	0.797	0.769	0.737	0.719
8	0.655	0.653	0.664	0.671	0.698	0.694	0.688	0.674	0.660	0.657	0.667
9	0.853	0.866	0.879	0.892	0.891	0.899	0.903	0.872	0.854	0.848	0.796
10	0.822	0.822	0.824	0.818	0.816	0.815	0.823	0.861	0.881	0.850	0.829